LAWRENCE
LIVERMORE
NATIONAL
LABORATORY

LLNL-JRNL-827712

On Analysis and Stochastic Modeling of the Particle Kinetic En- ergy Equation in Particle-Laden Isotropic Turbulent Flows

K. Pietryzk, J. Horwitz, F. Najjar, R. Minich

October 8, 2021

Physics of Fluids

Disclaimer

On Analysis and Stochastic Modeling of the Particle Kinetic Energy Equation in Particle-Laden Isotropic Turbulent Flows

Kyle Pietrzyk
Lawrence Livermore National Laboratory, 7000 East Ave., Livermore, CA 94550 and
Department of Energy Resources Engineering, Stanford University, 367 Panama St., Stanford, CA 94305

Jeremy Horwitz, Fady Najjar, and Roger Minich
Lawrence Livermore National Laboratory, 7000 East Ave., Livermore, CA 94550
(*pietrzyk@stanford.edu)
(Dated: December 9, 2021)

We analyze three-dimensional particle-laden, isotropic turbulence to develop an understanding of inertial particle dynamics from a kinetic energy perspective. Data trends implying inhomogeneous sampling of the flow by particles are identified and used to support a proposed particle behavior: particles appear to accumulate in regions of low flow kinetic energy over time because they lose kinetic energy and slow down in such regions, ultimately causing them to spend more time there. To elucidate this behavior, we derive a particle kinetic energy equation from the particle momentum equation, which incorporates inertial effects through the Schiller-Naumann drag correlation. Upon extracting fundamental physics from this equation, hypotheses regarding the role of the Stokes number in the temporal change of particle kinetic energy and the previously proposed particle behavior are evaluated using simulation data considering three Stokes numbers. Finally, a Fokker-Planck equation is used to derive the steady-state probability density function of the particle kinetic energy. The model fits the simulation data well and provides a tool for further investigation into understanding preferential concentration, as well as a reduced order model for predicting particle kinetic energy in turbulent flows.

I. INTRODUCTION

An interesting observation made in particle-laden turbulence is the tendency for inertial particles to cluster across multiple spatial and temporal scales [1]. The inhomogeneous particle concentration fields created by these accumulates serve as evidence for a phenomenon commonly referred to as *preferential concentration*. Due to the ubiquity of particle-laden turbulence throughout scientific disciplines, elements of preferential concentration have been reported in a range of studies involving droplet formation in clouds [2–4], spray combustion [5], and the coexistence of plankton species [6]. As such, a variety of methods have been used to quantify the presence of preferential concentration in a system and describe its qualitative features [7]. The results from these methods have allowed for the modeling of preferential concentration and have kept the analysis of its physical mechanisms an active area of research [8].

Central to the study of preferential concentration is the Stokes number, a dimensionless number that arises from the particle momentum equation as [9]

$$St = \frac{\hat{\tau}_p}{\hat{\tau}_{visc}}, \tag{1}$$

where $\hat{\tau}_p$ is the particle relaxation time and $\hat{\tau}_{visc}$ is the viscous time scale. In the extreme cases, particles are understood to act like *tracers* as $St \to 0$ and display a lack of influence from the flow as $St \to \infty$. This has led extensive efforts to focus on understanding the mechanisms behind preferential concentration in intermediate scenarios. Due to the number of variables involved in preferential concentration (e.g. particle size, particle shape, flow Reynolds number, domain geometry, etc.), a variety of perspectives from which to investigate the phenomenon exist. Here, we focus on studies that consider heavy, point-wise particles due to their relevance with the current investigation and applications involving sedimentation in rivers and the transport of sand, dust, or shrapnel through air.

Considering $St \ll 1$, Maxey [10] used an asymptotic analysis to find that regions of high strain-rates and low vorticities promote the accumulation of particles. This result was later found to agree with the numerical results of Squires and Eaton [1]. Qualitatively, the mechanism behind the results of Maxey has been understood as the expelling of small, heavy particles from the cores of vortices, or eddies, in the flow due to a centrifuging effect [11, 12]. Even at sub-Kolmogorov length scales, evidence of inertial particles sampling regions of high strain-rates rather than rotation has been observed [13]. This is in agreement with the results presented in the work of Zaichik and Alipchenkov [14], where improvements upon their statistical model for preferential concentration [15] allowed them to find that clustering increases with the ratio between rotation and strain-rate time scales. Together, these results offer a common understanding of preferential concentration at low values of $St \ll 1$.

As St increases ($St \sim 1$), the effects of preferential concentration become more evident with the formation of inertial particle clusters in the flow [16–18]. Significant efforts have been dedicated to understanding the mechanisms behind preferential concentration in this regime,

as the change in physics and abundance of observed trends offer opportunity to develop and compare new phenomenology [19]. For St ranging from 0.16 to 3.5, Bec *et al.* [20] investigated the acceleration statistics of inertial particles and found a tendency for particles with higher St to "filter" the influence of weak fluid velocities on the particle dynamics according to the particle response time. This description of particle behavior seems to agree with the accumulation behavior presented in the work of Yoshimoto and Goto [21], where small void regions are reported to initiate at low St, coexist with larger void regions at $St \sim 1$, and fade away as St increases further. Another phenomenology developed in the work of Gustavsson and Mehlig [22] describes *ergodic* and *non-ergodic* clustering mechanisms that compete at $St \sim 1$: clustering due to ergodic "multiplicative amplification" and clustering due to the previously described centrifuging effect at $St \ll 1$ (non-ergodic). The former mechanism is described as a dominant mechanism for large values of St [23] and has strong ties to the authors' continued series of work on clustering due to networks of *caustics* in the flow [24–26],

In another series of work, the idea of continuous clustering across temporal and spatial scales at zero-acceleration points in the flow was thoroughly investigated [27–29]. Upon extending the "sweep-stick" mechanism described in these works from 2D to 3D domains, the advantages of the mechanism for predicting particle clustering at high Stokes numbers over the centrifuging approach were highlighted [30]. Additionally, Obligado *et al.* [31] considered the sweep-stick mechanism and centrifuging effect with experimental data and found that the sweep-stick mechanism dominates for $St > 1$, while the centrifuging effect dominates for $St < 1$. Overall, more similarities were found between the sweep-stick mechanism and experimental evidence for the conditions considered in their analysis.

The wealth of investigations regarding preferential concentration from the perspectives of particle acceleration, spatial-temporal filtering, ergodic and non-ergodic mechanisms, and particle-flow structure interaction provide evidence of the extensive efforts dedicated to understanding the phenomenon. In this work, we consider another perspective and examine preferential concentration through the lens of flow and particle kinetic energies. Snapshots from three simulations of three-dimensional particle-laden, isotropic turbulence with differing Stokes numbers are analyzed and trends related to the flow and particle kinetic energies are elucidated. A description of particle behavior, where particles appear to accumulate in regions of low flow kinetic energy over time due to kinetic energy loss in such regions, is proposed based on the identified trends. An equation for the particle kinetic energy is then derived from the particle momentum equation, and the dynamics concerning idealized cases of particle kinetic energy increase and decrease are analyzed with support from the simulation data. The proposed particle behavior is then shown to be maintained over time in the simulation data, even at higher values of the Stokes number where single snapshots from the simulations do not display the proposed particle behavior.

Finally, scales that collapse the flow and particle kinetic energy probability density functions (PDFs) from the three simulations are determined. This intriguing behavior motivates the derivation of a simplified model for capturing the observed PDF. Previous simplified models related to preferential concentration have lowered computational costs and provided additional insight into the physics of the phenomenon for further investigations [14, 32]. In particular, a large number of statistical models have been successfully employed to accurately and efficiently study complex phenomena related to the dynamics of inertial particles and clustering [33–38]. Here, we derive the steady-state PDF of the particle kinetic energy using a Fokker-Planck model and show its agreement with the simulation data for optimized, but physical, noise parameters. Overall, this study provides an analysis of preferential concentration from the perspective of kinetic energy. In identifying temporal trends and deriving a model for the steady-state PDF of particle kinetic energy, a base for further investigation into preferential concentration from a kinetic energy perspective is provided.

The paper is organized as follows. In Section II, the simulation data, simulation methodology, and relevant averaging notation and nomenclature are described. Simulation statistics related to the flow and particle kinetic energies are then presented in Section III and used to propose a general behavior for the particle dynamics observed. In Section IV, an equation for the particle kinetic energy is derived from the particle momentum equation, and fundamental particle physics is extracted by analyzing cases of particle kinetic energy increase (Section IV A) and decrease (Section IV B) in time. Hypotheses of particle behaviors with respect to the Stokes number are also proposed, evaluated using the simulation data, and expanded upon in Section IV C. In Section V, the proposed particle behavior is shown to be present in the particle dynamics across multiple Stokes numbers, despite being difficult to observe in single snapshots of the simulation for high values of St. Finally, a Fokker-Planck equation is derived and solved in Section VI to provide a simplified model of the steady-state PDF for the particle kinetic energy. A summary of the work then follows in Section VII.

II. SIMULATION DATA AND METHODOLOGY

A. Simulation Data

We analyze the flow and particle kinetic energies extracted from three simulations of three-dimensional particle-laden, isotropic turbulence conducted in the work of Horwitz and Mani [9]. While a detailed account of the considered simulations may be found in their work,

we provide a concise description of the simulation parameters here. We note that larger data sets of differing parameters may also be used to conduct similar analyses to those presented in this work. Each simulation considers a cubic domain of fluid $\hat{\Omega}$ with an edge length of $128\hat{\eta}$, where $\hat{\eta}$ is the Kolmogorov length scale. The domain is meshed with $\sim 2 \times 10^6$ cells and periodic boundary conditions are applied. A velocity field $\hat{\mathbf{U}}\left(\hat{\mathbf{x}}, \hat{t}\right)$ is assumed to exist in the fluid, where $\hat{\mathbf{x}}$ is the displacement vector relative to a stationary origin in $\hat{\Omega}$ and $\hat{t}$ is the time. The Taylor Reynolds number considered for each simulation is $Re_\lambda = 33$. Particles are assumed to be point-wise with $\hat{d}_p < \hat{\eta}$, and much denser than the incompressible fluid with $\hat{\rho}_p \gg \hat{\rho}_f$, where $\hat{d}_p$ is the particle diameter, $\hat{\rho}_p$ is the particle density, and $\hat{\rho}_f$ is the fluid density. The Schiller-Naumann drag correlation is used to model the particle dynamics and all simulations are conducted in the *one-way coupling limit*, meaning the mass of the particles, $\hat{m}_p$, is small enough for particles to have no noticeable effects on the global fluid dynamics in the simulations. Due to small volume fractions ($\leq \mathcal{O}(10^{-5})$), no collision model is implemented in the simulations. While other specifications regarding each simulation may be found in Table I, including the total number of particles considered in each simulation $\mathcal{N}$, we note that snapshots from the simulations are roughly taken once every forcing time scale.

TABLE I. Additional simulation specifications for each data set considered.

Data Set	Total Snapshots	Volume Fraction	Stokes Number, St	Total Number of Particles, $\mathcal{N}$
1	184	25.0×10^{-6}	3.472	6408
2	161	8.33×10^{-6}	10.416	2136
3	184	2.78×10^{-6}	31.250	712

B. Particle Momentum Equation

To model the dynamics of inertial particles in turbulence, we consider the Schiller-Naumann drag correlation [9] and scale space by $\hat{\eta}$, time by the viscous time scale $\hat{\tau}_{visc} = \hat{\rho}_f \hat{\eta}^2 / \hat{\mu}$, where $\hat{\mu}$ is the fluid viscosity, and velocities by $\hat{\mathcal{U}} = \hat{\eta}/\hat{\tau}_{visc}$. Here and throughout the manuscript, hatted variables are assumed to be physically dimensional, while un-hatted variables are considered physically dimensionless. The particle momentum equation can then be written as

$$\frac{d\mathbf{v}}{dt} = \frac{f}{St}\left(\mathbf{u} - \mathbf{v}\right), \tag{2a}$$

$$\frac{d\mathbf{X}_p}{dt} = \mathbf{v}, \tag{2b}$$

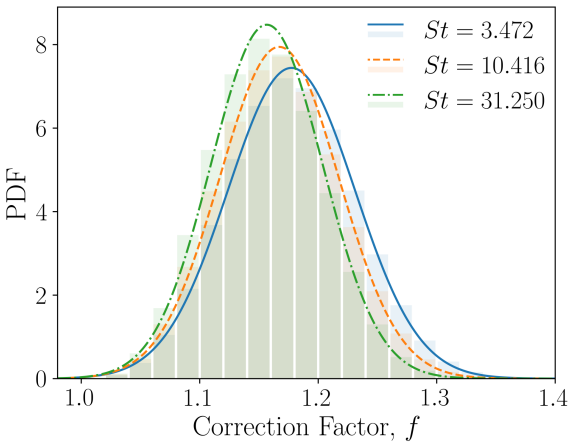

FIG. 1. Gaussian fit lines overlaying histograms of the correction factor f proposed by the Schiller-Naumann drag correlation. Samples are taken at all particle locations throughout time.

TABLE II. The averages and standard deviations of f from Figure 1.

Variable	$St = 3.472$	$St = 10.416$	$St = 31.250$
Average f	1.1785	1.1718	1.1660
Standard Deviation of f	0.05385	0.05139	0.04932

where $\mathbf{v} = \mathbf{v}(t)$ is the particle velocity, $\mathbf{u} = \mathbf{u}(t) = \mathbf{U}(\mathbf{X}_p(t), t)$ is the flow velocity evaluated at the particle location $\mathbf{X}_p(t)$, $f = \left(1 + 0.15 Re_p^{0.687}\right)$ is the correction factor proposed by the Schiller-Naumann drag correlation, and Re_p is the particle Reynolds number defined as

$$Re_p = \frac{\hat{\rho}_f \hat{\mathcal{U}} \hat{d}_p}{\hat{\mu}} \left|\mathbf{u} - \mathbf{v}\right|. \tag{3}$$

Additionally, we note that $\hat{\tau}_p = \hat{m}_p / (3\pi \hat{\mu} \hat{d}_p)$.

To supplement the Schiller-Naumann drag correlation, Figure 1 provides the PDF of the correction factor f from each data set, where samples of f are taken at all particle locations throughout time. As shown in Table II, the average value of f is roughly 1 for each data set, and the standard deviations of f are small with respect to the averages ($\sim 4.39\%$ of the average values). This point is used later to justify considering $f \sim 1$ in the analysis.

C. Averaging Notation and Nomenclature

To support the analysis, we define the following averaging notations

$$\langle\cdot\rangle_F = \frac{1}{\Omega}\int_\Omega (\cdot)\ d\mathbf{x}, \quad \langle\cdot\rangle_P = \frac{1}{N_p}\sum^{N_p}(\cdot), \quad \langle\cdot\rangle_T = \frac{1}{N_t}\sum^{N_t}(\cdot), \tag{4}$$

to denote an average taken over the non-dimensionalized domain (i.e., the fluid), an average taken over particles, and an average taken over snapshots in time, respectively. Here, N_p is the number of particles considered in the particle average and N_t is the number of snapshots considered in the time average.

We also denote the flow kinetic energy density as $K = \mathbf{U}\cdot\mathbf{U}$, the flow kinetic energy density at a particle location as $\mathscr{K} = \mathbf{u}\cdot\mathbf{u}$, and the particle kinetic energy density as $E = \mathbf{v}\cdot\mathbf{v}$. While both K and $\mathscr{K}$ have been scaled by $\hat{\rho}_f\hat{\mathcal{U}}^2/2$, we note that E has been scaled by $\hat{\rho}_p\hat{\mathcal{U}}^2/2$. Throughout the current work, we refer to K and $\mathscr{K}$ as values of the "flow kinetic energy" and to E as the "particle kinetic energy" for conciseness, since the flow kinetic energy and particle kinetic energy only differ from the corresponding energy densities by factors of constant volumes. Additional variables used in the text and figures, including the number of particles conditioned on different events and their ratios, are defined in Table III.

III. KINETIC ENERGY STATISTICS

To prompt the investigation, we consider ψ, the ratio of equally distributed points in the domain experiencing $K < \langle K\rangle_F$ at an instance in time, and α, the ratio of particles experiencing $\mathscr{K} < \langle K\rangle_F$ at an instance in time (i.e., $\mathcal{N}_{\mathscr{K}<\langle K\rangle_F}/\mathcal{N}$, where $\mathcal{N}_{\mathscr{K}<\langle K\rangle_F}$ is the number of particles experiencing $\mathscr{K} < \langle K\rangle_F$ at an instance in time and $\mathcal{N}$ is the total number of particles in the simulation). Samples of ψ and α are taken throughout time to create the histograms shown in Figure 2, and Gaussian fit lines are used to approximate the PDFs. As reported in Table IV for $\langle\psi\rangle_T$, the average ratios of the domain experiencing $K < \langle K\rangle_F$ for $St = 3.472$, 10.416, and 31.250 are 59.26%, 59.28%, and 59.13%, respectively. However, the reported values for $\langle\alpha\rangle_T$ suggest that the average ratio of particles residing in these regions are 67.06%, 68.36%, and 68.80%. The imbalance in statistics between $\langle\psi\rangle_T$ and $\langle\alpha\rangle_T$ for each value of St suggests that a bias exists in the sampling of the flow by the particles with respect to $\langle K\rangle_F$.

To probe this trend further, we introduce "$\mathbf{v}\cdot d\mathbf{v}/dt$", the dot product between the particle velocity and acceleration vectors, as a measure of general alignment ($\mathbf{v}\cdot d\mathbf{v}/dt > 0$), or "anti-alignment" ($\mathbf{v}\cdot d\mathbf{v}/dt < 0$) between the two vectors. By applying the chain rule, this quantity is identified as half the temporal derivative of the particle kinetic energy, or

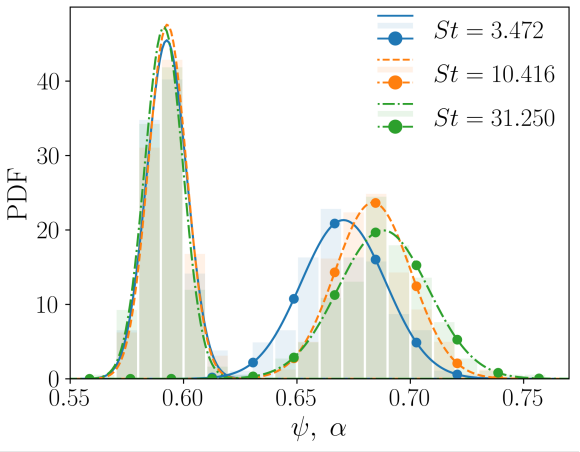

FIG. 2. Gaussian fit lines overlaying histograms of ψ (lines without overlaid dots) and α (lines with overlaid dots) sampled throughout time.

$$\frac{dE}{dt} = 2\mathbf{v}\cdot\frac{d\mathbf{v}}{dt}. \tag{5}$$

It then follows that general alignment between particle velocity and acceleration vectors coincides with a particle kinetic energy increase ($dE/dt > 0$), and general anti-alignment coincides with a particle kinetic energy decrease ($dE/dt < 0$).

By analyzing the relationship between dE/dt and the flow regions sampled by the particles with respect to $\langle K\rangle_F$, an intriguing trend is found. In Figure 3(a), we consider β, the ratio of particles losing kinetic energy at an instance in time (i.e., $\mathcal{N}^-/\mathcal{N}$, where $\mathcal{N}^-$ is the number of particles losing kinetic energy at an instance in time). Samples of β are taken throughout time to generate the displayed histograms, and Gaussian fit lines are used to approximate the displayed PDFs. As reported in Table IV for $\langle\beta\rangle_T$, the average ratios of particles losing kinetic energy at a given time for $St = 3.472$, 10.416, and 31.250 are 45.86%, 51.37%, and 59.38%, respectively. Assuming the system is statistically stationary, finding $\langle\beta\rangle_T < 50.00\%$ for $St = 3.472$ implies that the time intervals over which particles gain kinetic energy are longer than those over which they lose kinetic energy, a behavior that agrees with the previously studied *slow gain* and *fast loss* phenomenon [39]. However, finding $\langle\beta\rangle_T > 50.00\%$ for $St = 10.416$ and 31.250 implies the opposite behavior (i.e, the time intervals over which particles gain kinetic energy are *shorter* than those over which they lose kinetic energy) and points to potentially fruitful investigations regarding high St dynamics. Despite the trend of increasing $\langle\beta\rangle_T$ with St, we note that the values of $\langle\beta\rangle_T$ amount to roughly half of the particles in the domain losing kinetic energy, and therefore half of the particles in the domain gaining kinetic energy, at a given time for each value of St considered.

TABLE III. The nomenclature used throughout the text and figures of the current work.

Nomenclature	
Variable	Definition
K	Dimensionless flow kinetic energy, $\mathbf{U}\cdot\mathbf{U}$.
$\langle K\rangle_F$	Dimensionless domain-averaged flow kinetic energy.
$\mathscr{K}$	Dimensionless flow kinetic energy at the particle location, $\mathbf{u}\cdot\mathbf{u}$.
E	Dimensionless particle kinetic energy, $\mathbf{v}\cdot\mathbf{v}$.
$\langle E\rangle_P$	Dimensionless particle-averaged particle kinetic energy.
$\mathcal{N}$	Total number of particles.
$\mathcal{N}_{\mathscr{K}<\langle K\rangle_F}$	The number of particles experiencing $\mathscr{K}<\langle K\rangle_F$ at an instance in time.
$\mathcal{N}^-$	The number of particles losing kinetic energy at an instance in time.
$\mathcal{N}^+$	The number of particles gaining kinetic energy at an instance in time.
$\mathcal{N}^-_{\mathscr{K}<\langle K\rangle_F}$	The number of particles experiencing $\mathscr{K}<\langle K\rangle_F$ and losing kinetic energy at an instance in time.
$\mathcal{N}^+_{\mathscr{K}<\langle K\rangle_F}$	The number of particles experiencing $\mathscr{K}<\langle K\rangle_F$ and gaining kinetic energy at an instance in time.
$\mathcal{N}^-_s$	The number of particles experiencing a strong event of particle kinetic energy decrease at an instance in time.
ψ	The ratio of equally distributed points in the domain experiencing $K<\langle K\rangle_F$ at an instance in time.
α	The ratio of particles experiencing $\mathscr{K}<\langle K\rangle_F$ at an instance in time (i.e., $\mathcal{N}_{\mathscr{K}<\langle K\rangle_F}/\mathcal{N}$).
β	The ratio of particles losing kinetic energy at an instance in time (i.e., $\mathcal{N}^-/\mathcal{N}$).
κ^-	The ratio of particles experiencing $\mathscr{K}<\langle K\rangle_F$ and losing kinetic energy out of the particles losing kinetic energy at an instance in time (i.e., $\mathcal{N}^-_{\mathscr{K}<\langle K\rangle_F}/\mathcal{N}^-$).
κ^+	The ratio of particles experiencing $\mathscr{K}<\langle K\rangle_F$ and gaining kinetic energy out of the particles gaining kinetic energy at an instance in time (i.e., $\mathcal{N}^+_{\mathscr{K}<\langle K\rangle_F}/\mathcal{N}^+$).
γ_l	The ratio between the average particle kinetic energy of particles experiencing $\mathscr{K}<\langle K\rangle_F$ and the average particle kinetic energy at an instance in time (i.e., $\langle E\vert_{\mathscr{K}<\langle K\rangle_F}\rangle_P/\langle E\rangle_P$).
γ_g	The ratio between the average particle kinetic energy of particles experiencing $\mathscr{K}>\langle K\rangle_F$ and the average particle kinetic energy at an instance in time (i.e., $\langle E\vert_{\mathscr{K}>\langle K\rangle_F}\rangle_P/\langle E\rangle_P$).
ξ	The ratio of particles experiencing strong events out of the particles losing kinetic energy at an instance in time (i.e., $\mathcal{N}^-_s/\mathcal{N}^-$).

With this in mind, we consider κ^+, the ratio of particles experiencing $\mathscr{K}<\langle K\rangle_F$ out of the particles gaining kinetic energy (i.e., $\mathcal{N}^+_{\mathscr{K}<\langle K\rangle_F}/\mathcal{N}^+$, where $\mathcal{N}^+_{\mathscr{K}<\langle K\rangle_F}$ is the number of particles experiencing $\mathscr{K}<\langle K\rangle_F$ and gaining kinetic energy at an instance in time and $\mathcal{N}^+$ is the number of particles gaining kinetic energy at an instance in time), and κ^-, the ratio of particles experiencing $\mathscr{K}<\langle K\rangle_F$ out of the particles losing kinetic energy (i.e., $\mathcal{N}^-_{\mathscr{K}<\langle K\rangle_F}/\mathcal{N}^-$, where $\mathcal{N}^-_{\mathscr{K}<\langle K\rangle_F}$ is the number of particles experiencing $\mathscr{K}<\langle K\rangle_F$ and losing kinetic energy at an instance in time). Samples of κ^+ and κ^- are taken throughout time to create the histograms shown in Figure 3(b), and Gaussian fit lines are used to approximate the PDFs. As reported in Table IV for $\langle\kappa^+\rangle_T$, the average ratios of particles experiencing $\mathscr{K}<\langle K\rangle_F$ out of the particles gaining kinetic energy for $St=3.472$, 10.416, and 31.250 are 51.98%, 49.18%, and 54.13%, respectively. These values are similar to the average ratios of equally distributed points in the domain experiencing $K<\langle K\rangle_F$, $\langle\psi\rangle_T$, with a 7.46% difference on average. This indicates that particles gaining kinetic energy sample K relatively uniformly with respect to $\langle K\rangle_F$; however, the same is not true for particles losing kinetic energy. As reported in Table IV for $\langle\kappa^-\rangle_T$, the average ratios of particles experiencing $\mathscr{K}<\langle K\rangle_F$ out of the particles losing kinetic energy for $St=3.472$, 10.416, and 31.250 are 84.85%, 86.51%, and 78.84%, respectively. These values are much greater than $\langle\psi\rangle_T$ corresponding to each data set, with a 24.18% difference on average. This indicates that a majority of particles losing kinetic energy are sampling the flow in regions of low K with respect to $\langle K\rangle_F$.

In light of the values of $\langle\beta\rangle_T$, $\langle\kappa^+\rangle_T$, and $\langle\kappa^-\rangle_T$, the domain-sampling bias of particles seen in Figure 2 seems to be induced in-part by the accumulation of particles losing kinetic energy in flow regions where $K<\langle K\rangle_F$. Further evidence for this hypothesis may be gleaned from considering γ_l, the ratio between the average particle kinetic energy of particles experiencing $\mathscr{K}<\langle K\rangle_F$ and the average particle kinetic energy at an instance in time (i.e., $\langle E\vert_{\mathscr{K}<\langle K\rangle_F}\rangle_P/\langle E\rangle_P$), and γ_g, the ratio between the

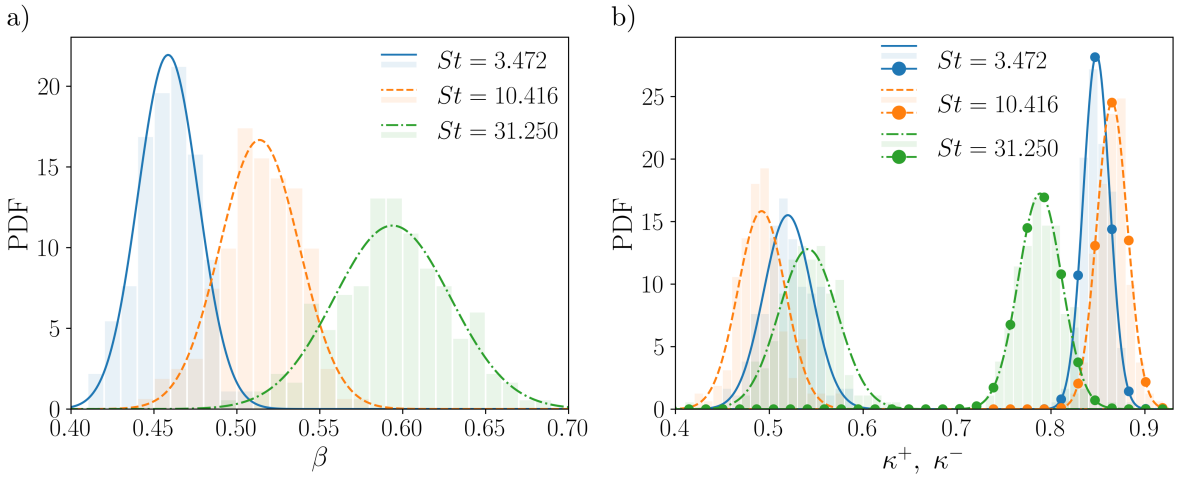

FIG. 3. a) Gaussian fit lines overlaying histograms of β sampled throughout time. b) Gaussian fit lines overlaying histograms of κ^+ (lines without overlaid dots) and κ^- (lines with overlaid dots) sampled throughout time.

TABLE IV. A summary of the temporally averaged ratios (defined in Table III) from Figures 2, 3, 4, and 6 for the three considered values of St.

Variable	$St = 3.472$	$St = 10.416$	$St = 31.250$
$\langle\psi\rangle_T$	0.5926	0.5928	0.5913
$\langle\alpha\rangle_T$	0.6706	0.6836	0.6880
$\langle\beta\rangle_T$	0.4586	0.5137	0.5938
$\langle\kappa^+\rangle_T$	0.5198	0.4918	0.5413
$\langle\kappa^-\rangle_T$	0.8485	0.8651	0.7884
$\langle\gamma_l\rangle_T$	0.6545	0.7726	0.8816
$\langle\gamma_g\rangle_T$	1.7058	1.4928	1.2621
$\langle\xi\rangle_T$	0.3400	0.5837	0.8033

average particle kinetic energy of particles experiencing $\mathscr{K} > \langle K\rangle_F$ and the average particle kinetic energy at an instance in time (i.e., $\langle E|_{\mathscr{K}>\langle K\rangle_F}\rangle_P/\langle E\rangle_P$). Samples of γ_l and γ_g are taken throughout time to create the histograms shown in Figures 4(a) and 4(b), and Gaussian fit lines are used to approximate the PDFs. As reported in Table IV, $\langle\gamma_l\rangle_T$ is 65.45%, 77.26%, and 88.16% and $\langle\gamma_g\rangle_T$ is 170.58%, 149.28%, and 126.21% for $St = 3.472$, 10.416, and 31.250, respectively. While both $\langle\gamma_l\rangle_T$ and $\langle\gamma_g\rangle_T$ become similar to 1 as St increases, the statistics suggest that particles in regions of low flow kinetic energy have low E with respect to $\langle E\rangle_P$, and particles in regions of high flow kinetic energy have high E with respect to $\langle E\rangle_P$.

Altogether, the previous results indicate that 1.) a majority of particles losing kinetic energy reside in regions of low flow kinetic energy, and 2.) particles in regions of low flow kinetic energy generally have low E with respect to $\langle E\rangle_P$ (i.e., they move slowly). In combining these ideas, we propose the following particle behavior, depicted in Figure 5: particles losing kinetic energy are often found in regions of low flow kinetic energy. Because of their energy loss, these particles begin to move slowly through the low flow kinetic energy regions (i.e., at velocities similar to the low flow velocities) and end up spending the most amount of time there. Ultimately, an accumulation-like behavior in low flow kinetic energy regions is displayed over time. Additionally, finding that particles move quickly in high flow kinetic energy regions (Figure 4(b)) only enhances the appearance of clustering, as particles will quickly leave the regions of high flow kinetic energy and slow down with other particles in regions of low flow kinetic energy. Due to the similarities recognized, we propose that this behavior directly relates preferential concentration with the dynamics observed in "flight-crash" events [40, 41], where fluid particles suddenly decelerate in low flow kinetic energy regions, for low values of St.

IV. PARTICLE KINETIC ENERGY EQUATION

In light of the proposed particle behavior and supporting statistics, a particle kinetic energy equation for a single particle is now derived and analyzed to detail the relationship between the particle behavior and St. To this end, we combining equations (2a) and (5), such that [42]

$$\frac{dE}{dt} = \frac{2f}{St}\left(\mathbf{u}\cdot\mathbf{v} - E\right). \tag{6}$$

A definition for $\mathbf{u}\cdot\mathbf{v}$ is obtained by dotting each side of equation (2a) with itself. In simplifying the result, we gain

$$\mathbf{u}\cdot\mathbf{v} = \frac{1}{2}\left[\mathscr{K} + E - \frac{St^2}{f^2}\frac{d\mathbf{v}}{dt}\cdot\frac{d\mathbf{v}}{dt}\right]. \tag{7}$$

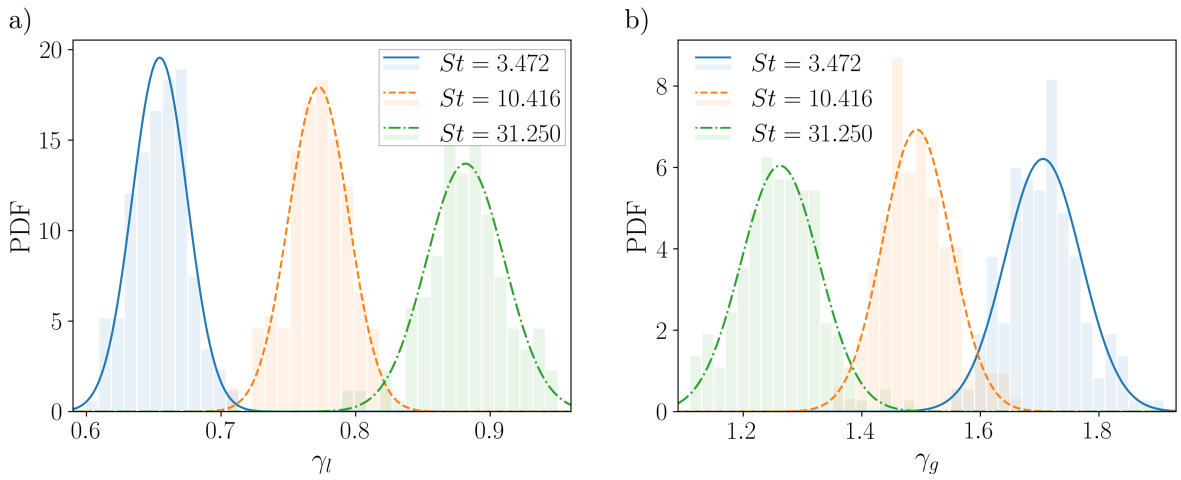

FIG. 4. a) Gaussian fit lines overlaying histograms of γ_l sampled throughout time. b) Gaussian fit lines overlaying histograms of γ_g sampled throughout time.

Substituting equation (7) into equation (6) then obtains

$$\frac{dE}{dt} = \underbrace{\frac{f}{St}\left(\mathscr{K} - E\right)}_{\text{Kinetic Energy Difference}} \underbrace{- \frac{St}{f}\frac{d\mathbf{v}}{dt}\cdot\frac{d\mathbf{v}}{dt}}_{\text{Dissipation}}. \tag{8}$$

Equation (8) provides dE/dt in terms of $\mathscr{K}$, E, and $d\mathbf{v}/dt$. While it is similar to previous equations used for modeling the evolution of the granular temperature [37, 43], it is worth emphasizing that this equation was derived directly from the particle momentum equation and describes the time evolution of the particle kinetic energy for a single particle. The two terms on the right-hand side of equation (8) are identified as 1.) the difference between the flow kinetic energy at the particle location and the particle kinetic energy, and 2.) a particle kinetic energy dissipation term. Interestingly, this deterministic equation for the kinetic energy of a single particle bears resemblance to the granular temperature equation derived in the work of Garzó *et al.* [44], where the particle phase is treated in a probabilistic fashion.

Fundamental particle behaviors can be extracted from equation (8) by analyzing how the equation allows the particle kinetic energy to change in time, an idea inspired by the quadrant analysis provided in the work of Zhao *et al.* [45]. Idealized cases where $\mathscr{K} > E$ and $\mathscr{K} < E$ are now discussed for $dE/dt > 0$ and $dE/dt < 0$. Additionally, since f and St appear as a ratio in equation (8), we let $f \sim 1$ (see Table II) and focus on the effect of St without loss of generality.

A. Case I: Increasing Particle Kinetic Energy, $dE/dt > 0$

To begin, equation (8) is analyzed assuming $dE/dt > 0$. Because the dissipation term in equation (8) is always negative, the case of $\mathscr{K} < E$ cannot exist, as a positive value is needed on the right-hand side to balance the equation. Therefore, only when $\mathscr{K} > E$ does particle kinetic energy increase in time. In general, this behavior implies that the particle speed increases in regions with high flow kinetic energy. As a result, we hypothesize that particles will tend to quickly pass through these regions.

B. Case II: Decreasing Particle Kinetic Energy, $dE/dt < 0$

Considering $dE/dt < 0$, we find that both cases where $\mathscr{K} > E$ and $\mathscr{K} < E$ can exist. We will refer to these cases as *strong events* and *weak events* of particle kinetic energy decrease, respectively. In general, we note that the particle speed decreases in either event.

For strong events ($\mathscr{K} > E$), we analyze equation (8) for cases of small and large St independently. For small St ($St < 1$), we conclude that $|d\mathbf{v}/dt|$ must be large in order for the dissipation term (multiplied by St) to balance the kinetic energy difference (positive and multiplied by $1/St$) with the negative left-hand side of the equation ($dE/dt < 0$). In accordance with equation (5), this suggests that generally anti-aligned particle velocity and acceleration vectors ($dE/dt < 0$) will quickly realign ($dE/dt > 0$) for small St due to large $|d\mathbf{v}/dt|$. This behavior is consistent with that of fluid and low-St particles in "flight-crash" events [40, 41], and with the qualitative understanding that particles closely follow the flow with short "particle response times" at lower values of St [8]. Therefore, when St is small, we hypothesize that particles will spend little time experiencing strong events due to their tendency to quickly evolve into cases where $dE/dt > 0$.

As St increases, we hypothesize that the tendency for particle velocity and acceleration vectors to realign is

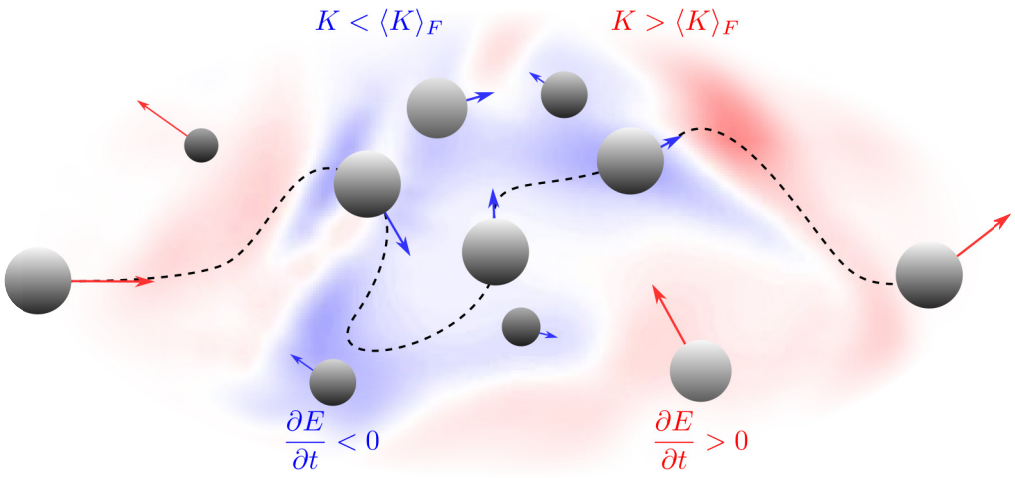

FIG. 5. A depiction of the proposed particle behavior. As shown, particles losing kinetic energy are often found in regions of low flow kinetic energy. Due to their energy loss, these particles move slowly through such regions, and ultimately spend the most amount of time there. This causes particles to display an accumulation-like behavior in regions of low flow kinetic energy over time.

maintained, but the magnitude of the acceleration vector $|d\mathbf{v}/dt|$ is reduced. According to equation (8), because increasing St reduces the magnitude of the kinetic energy difference and increases the magnitude of the dissipation term, the magnitude of the acceleration vector $|d\mathbf{v}/dt|$ for balancing the equation is smaller than in the case of small St. As a result, anti-aligned particle velocity and acceleration vectors realign slower, in agreement with the understanding that for increasing St, particles exhibit longer particle response times and deviate further from the flow trajectory [46]. Therefore, as St increases, we hypothesize that particles will spend more time experiencing strong events, if enabled by the spatial-temporal scales of the flow.

For weak events ($\mathscr{K} < E$), it is sufficient to note that the particle speed reduces. As a result, particles are slowed as they pass through regions of low flow kinetic energy.

C. Analysis of Strong Events

We now provide supporting evidence for the previous hypotheses regarding the amount of time particles experience strong events for varying St. As shown in Figure 6, we consider ξ, the ratio of strong events to all particle kinetic energy decreasing events at an instance in time (i.e., $\mathcal{N}_s^-/\mathcal{N}^-$, where $\mathcal{N}_s^-$ is the number of particles experiencing a strong event of particle kinetic energy decrease at an instance in time). Samples of ξ are taken throughout time to generate the displayed histograms, and Gaussian fit lines are used to approximate the displayed PDFs. As reported in Table IV for $\langle \xi \rangle_T$, the average ratios of particles undergoing strong events to all particle kinetic energy decreasing events for $St = 3.472$, 10.416, and 31.250 are 34.00%, 58.37%, and 80.33%, respectively. The large increase in the number of strong events counted throughout time with increasing St agrees with the previous hypotheses made from analyzing equation (8).

In light of the understanding gained from equation (8) and the supporting trend found in Figure 6, we deduce that the number of strong events sampled over time provides a measure for how closely particles follow the spatial-temporal scales of the flow, similar to that provided by St and the particle response time. In particular, as St and the number of strong events recorded over time increase, it is understood that high flow velocities and long spatial-temporal scales in the flow begin to influence the particle dynamics more than low flow velocities and short spatial-temporal scales in the flow. Previous research has provided various descriptions of this idea with similar evidence, including the *velocity filtering* effect proposed by Bec *et al.* [20] at higher values of St and the *vanishing* of small void regions reported by Yoshimoto and Goto [21] as St increases. In general, the effects of low flow velocities and short spatial-temporal scales in the flow become less noticeable in the particle dynamics as St increases, until particles exhibit no noticeable response to flow signals at these scales.

Despite the lack in particle response to short spatial-temporal scales in the flow at high St, the statistics in Figures 2, 3, and 4 provide clear evidence at all three considered values of St for the proposed particle behavior, which ultimately depends on particles being responsive to the flow. To resolve the perceived contradiction, we emphasize that while particles with high St may lack response to shorter spatial-temporal signals from the flow, they maintain responsiveness to longer spatial-temporal signals. As a result, particles with high St may look as though they do not follow the flow on shorter scales, but at longer scales, they should appear to follow the flow. In a similar manner, the proposed particle behavior may

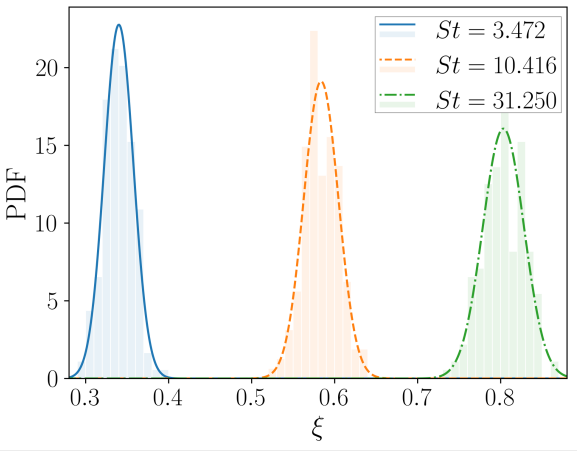

FIG. 6. Gaussian fit lines overlaying histograms of ξ sampled throughout time.

not be obvious on shorter time scales for high values of St; however, we speculate that if particles are observed over a sufficiently long time scale, the proposed behavior may be observed with enough samples. This proposition adheres to there being sufficiently large spatial-temporal scales present in the flow for a given value of St, such that particles do not lack responsiveness to the flow in total. It also adheres to the value of St being large enough, such that particles can deviate from the flow trajectory and begin exhibiting clustering behavior.

V. INSTANTANEOUS VS. TIME-AVERAGED PARTICLE BEHAVIOR

We now provide evidence that the proposed particle behavior is maintained for high values of St over long temporal scales, despite being difficult to observe at instances in time. As shown in Figure 7, subfigures are paired by their values of St: Figures 7(a) and 7(b) correspond to $St = 3.472$, Figures 7(c) and 7(d) correspond to $St = 10.416$, and Figures 7(e) and 7(f) correspond to $St = 31.250$. In each pair of subfigures, two z-slices of the domain distanced roughly 55 Kolmogorov length scales apart (roughly half the domain edge length) are shown at a single instance in time. For each z-slice, a blue-hued contour denotes $\langle K \rangle_z$, the average value of K in the z-direction within $z = \pm 4$ of the considered z-slice. Additionally, particles within $z = \pm 4$ of the considered z-slice are projected onto the analyzed plane as points and colored by a red-hued contour according to their values of E. Both $\langle K \rangle_z$ and E from each z-slice have been scaled by $\sigma(K)$, the standard deviation of K in the entire domain at the corresponding time instance.

As shown in Figures 7(a) and 7(b) for $St = 3.472$, particles tend to reside in lighter hued regions of the $\langle K \rangle_z$-contours and display lighter hues in the E-contours. These results are consistent with the previously described particle behavior: particles tend to reside in regions of low K because they move slowly in such regions and spend the most time in them. Additionally, particles residing near darker hues of the $\langle K \rangle_z$-contours tend to display darker hues in the E-contours. This is in alignment with the results of Figure 4(b), where particles experiencing $\mathscr{K} > \langle K \rangle_F$ tend to also have high values of E. It is worth emphasizing that not all particles in Figures 7(a) and 7(b) follow the described coloring configurations (e.g., particles near the bottom-left corners display lighter hues in darker hued regions of the $\langle K \rangle_z$-contours). While these cases are direct evidence that the proposed particle behavior may be difficult to observe at single instances in time, later results will show that the proposed particle behavior is still maintained over longer temporal scales. In general, however, a majority of the particles in Figures 7(a) and 7(b) are observed to follow the proposed particle behavior at the provided instances in time and display an accumulation-like behavior within regions of low flow kinetic energy.

For $St = 10.416$, the particles in Figures 7(c) and 7(d) appear to follow the proposed particle behavior much less. As shown, particles are distributed more homogeneously and do not seem to show a strong trend between the hues of the $\langle K \rangle_z$-contour and the hues of the E-contour. This behavior is in correspondence with the hypothesis that as St increases, the proposed particle behavior becomes difficult to observe on short time scales (i.e., single snapshots) due to the lack in response of particles to shorter spatial-temporal signals in the flow.

A similar observation is made for $St = 31.250$ in Figures 7(e) and 7(f), where particles are also distributed homogeneously and with no obvious trends between the hues of the $\langle K \rangle_z$-contours and the hues of the E-contours. While the reduced number of particles for $St = 31.250$ seems to contribute to the observed homogeneous distribution, we emphasize that evidence of this distribution is already seen in Figures 7(c) and 7(d) for $St = 10.416$. Further, the distribution is only expected to become more obvious for higher values of St, as this is the trend seen in previous literature [28, 47, 48].

As the proposed particle behavior becomes more difficult to observe in a single time instance for increasing St, we maintain that the particle behavior is observed over long enough time scales with enough samples. In Figure 8, we consider PDFs of the flow kinetic energy sampled at all particle locations throughout time, $\mathscr{K}/\langle\langle K \rangle_F\rangle_T$, and the flow kinetic energy sampled at equally distributed points in the domain throughout time, $K/\langle\langle K \rangle_F\rangle_T$. As shown, the PDFs of $\mathscr{K}/\langle\langle K \rangle_F\rangle_T$ and $K/\langle\langle K \rangle_F\rangle_T$ are independently similar for all values of St. Additionally, when the scaled flow kinetic energy is less than ~ 1, the PDFs sampling $\mathscr{K}/\langle\langle K \rangle_F\rangle_T$ have higher PDF values than those sampling $K/\langle\langle K \rangle_F\rangle_T$. This demonstrates that particles tend to reside in regions of low flow kinetic energy when compared to a homogeneous sampling of the flow kinetic energy in the domain, which is in correspondence with the previous observations in Figure 2

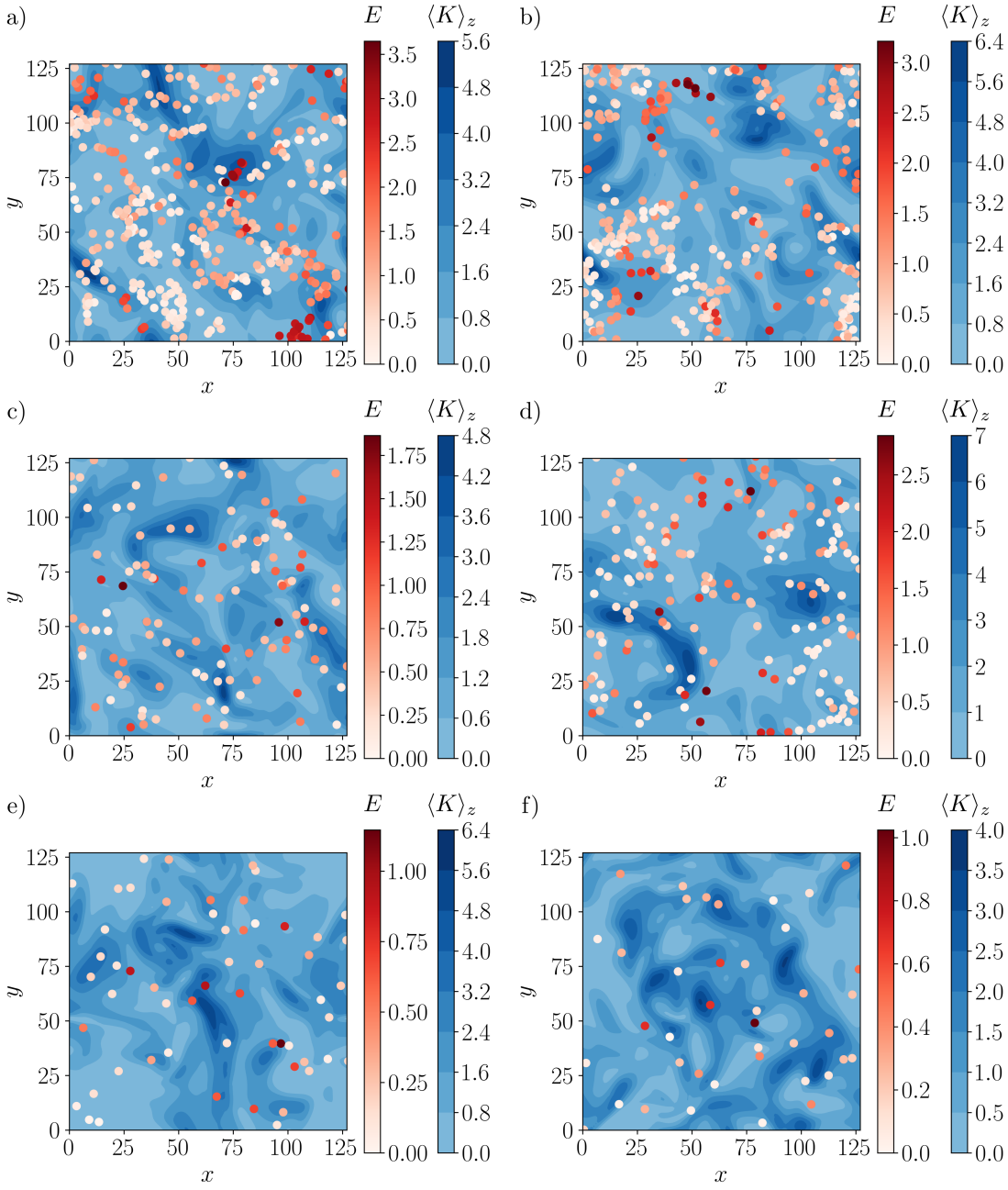

FIG. 7. Contour plots of $\langle K\rangle_z$ (blue-hued) and E (red-hued) for $St = 3.472$ ((a) and (b)), $St = 10.416$ ((c) and (d)), and $St = 31.250$ ((e) and (f)). For corresponding values of St, contours are taken at the same instance in time on z-slices distanced roughly half of the domain edge length apart. $\langle K\rangle_z$ is the averaged value of K over $z = \pm 4$ relative to the considered z-slices. Points represent particles within $z = \pm 4$ of the considered z-slices. Here, $\langle K\rangle_z$ and E are scaled by $\sigma(K)$ and $(\hat{\rho}_f/\hat{\rho}_p)\sigma(K)$, respectively, where $\sigma(K)$ is the standard deviation of K in the entire domain at the corresponding time instance. In (a) and (b), $\sigma(K) = 0.7594\langle K\rangle_F$; in (c) and (d), $\sigma(K) = 0.7865\langle K\rangle_F$; in (e) and (f), $\sigma(K) = 0.8078\langle K\rangle_F$.

and the proposed particle behavior. Therefore, despite the difficulty in observing the proposed particle behavior on short time scales for high values of St (Figures 7(c) - 7(f)), particles still follow the behavior, as they tend to spend the most amount of time in regions of low K due to kinetic energy loss in such regions.

In light of these results, we conjecture that the proposed particle behavior can be observed for higher values of St on longer spatial-temporal scales, granted long enough signals are received by particles from the flow. In the case where such signals are not present in a simulated or experimentally acquired flow, the particle behavior may not be observed and particles may seem to ignore the flow throughout time. Nonetheless, a finite

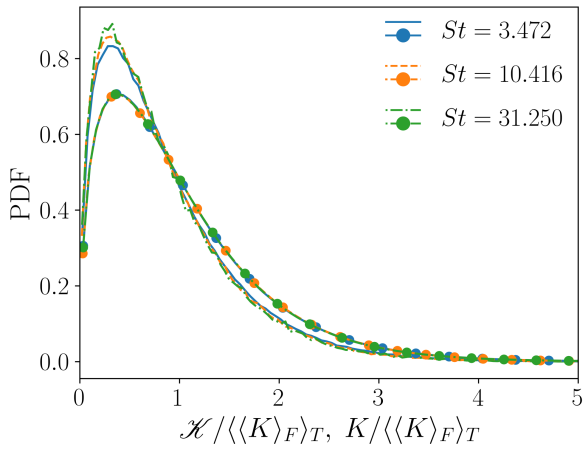

FIG. 8. The PDFs for $\mathscr{K}/\langle\langle K\rangle_F\rangle_T$ (lines without overlaid dots) and $K/\langle\langle K\rangle_F\rangle_T$ (lines with overlaid dots).

value of St suggests a time scale over which the proposed particle behavior may be observed exists.

VI. A FOKKER-PLANCK MODEL FOR STEADY-STATE PARTICLE KINETIC ENERGY

Seeing that the PDFs of $\mathscr{K}/\langle\langle K\rangle_F\rangle_T$ and $K/\langle\langle K\rangle_F\rangle_T$ in Figure 8 are independently similar for the considered values of St, a scale for E is pursued such that the PDFs sampling scaled E from all particles throughout time collapse to a similar PDF. As shown in Figure 9(a), the analogous scale $\langle\langle E\rangle_P\rangle_T$ is found not only to collapse the PDFs of $E/\langle\langle E\rangle_P\rangle_T$, but collapse these PDFs onto the PDFs of $K/\langle\langle K\rangle_F\rangle_T$. This motivates the search for another scale that collapses scaled $\mathscr{K}$ onto the PDFs of $K/\langle\langle K\rangle_F\rangle_T$ and $E/\langle\langle E\rangle_P\rangle_T$, which is found to be $\langle\langle \mathscr{K}\rangle_P\rangle_T$ as shown in Figure 9(a).

Because the data for $\mathscr{K}$, K, and E throughout time for the considered values of St collapse onto similar PDFs under various scales, we find it useful to provide a model for the steady-state PDFs seen in Figure 9(a). In recent literature, stochastic models have demonstrated their abilities to track evolving granular temperatures [37, 43] and relative motion PDFs of particle pairs [49–51]. Here, we use equations (2a) and (6) to derive a Fokker-Planck equation for $\tilde{E} = E/\langle\langle E\rangle_P\rangle_T$, the scaled particle kinetic energy for a single particle, from which the steady-state PDF may be found. Assuming $f \sim 1$ due to the results in Table II, we consider colored noise in $\mathbf{u}(t)$ and formulate a Fokker-Planck equation [52] from the following system of ordinary differential equations:

$$\frac{d\tilde{E}(t)}{dt} = -\frac{2}{St}\tilde{E}(t) + \frac{2}{St}\tilde{\mathbf{u}}(t)\cdot\tilde{\mathbf{v}}(t), \tag{9a}$$

$$\frac{d\tilde{\mathbf{v}}(t)}{dt} = -\frac{1}{St}\tilde{\mathbf{v}}(t) + \frac{1}{St}\tilde{\mathbf{u}}(t), \tag{9b}$$

$$\frac{d\tilde{\mathbf{u}}(t)}{dt} = -\frac{1}{\tau}\tilde{\mathbf{u}}(t) + \frac{D^{\frac{1}{2}}}{\tau}\mathbf{Q}(t), \tag{9c}$$

where $\tilde{\mathbf{v}}(t) = \mathbf{v}(t)/(\langle\langle E\rangle_P\rangle_T)^{1/2}$, $\tilde{\mathbf{u}}(t) = \mathbf{u}(t)/(\langle\langle E\rangle_P\rangle_T)^{1/2}$, $\mathbf{Q}(t)$ is scaled Gaussian white noise, and τ and $D^{1/2}$ are parameters used to describe the colored noise [53]. We note that the Ornstein-Uhlenbeck model in equation (9c) allows us to account for non-instantaneous correlations in $\tilde{\mathbf{u}}(t)$. In the limit of the time scale ratio $\tau \to 0$, $\tilde{\mathbf{u}}(t)$ reduces to delta-correlated noise. We also note that $\mathbf{Q}(t)$ takes on typical properties of Gaussian white noise, namely [54]

$$\overline{Q_i(t)} = 0, \quad \overline{Q_i(t_1)Q_j(t_2)} = C_1\delta_{ij}\delta(t_1 - t_2), \tag{10}$$

where C_1 is a constant, $\overline{(\cdot)}$ denotes an ensemble average, and $\delta(t_1 - t_2)$ and $\delta_{ij} = \mathbf{I}$ are forms of the Dirac delta function. In general, we write the Fokker-Planck equation for $\tilde{E}$ as [52]

$$\frac{\partial W\left(\tilde{E},\tilde{t}\right)}{\partial\tilde{t}} = -\frac{\partial}{\partial\tilde{E}}\left[D^{(1)}\left(\tilde{E},\tilde{t}\right)W\left(\tilde{E},\tilde{t}\right)\right] + \frac{\partial^2}{\partial\tilde{E}^2}\left[D^{(2)}\left(\tilde{E},\tilde{t}\right)W\left(\tilde{E},\tilde{t}\right)\right], \tag{11}$$

where $W(\tilde{E},\tilde{t})$ is the PDF of $\tilde{E}$, $\tilde{t} = \tau^{-1/2}t$ is a rescaled time, and $D^{(1)}(\tilde{E},\tilde{t})$ and $D^{(2)}(\tilde{E},\tilde{t})$ are the drift and diffusion coefficients, respectively. We note that the adopted stochastic model does not account for spatial correlations in particle positions, nor correlations in fluid fluctuations driving the particle motion. Future work could investigate augmenting the current model to account for spatially correlated noise, which has recently been shown to improve stochastic predictions of particle clustering [51].

While the details may be found in Appendix A, our derivation only considers long times after the initial state of the system, and assumes $(3\tau^{1/2}/St + 1/\tau^{1/2})^{-1} \ll 1$ to neglect terms multiplied by $\partial^2\tilde{E}(t)/\partial t^2$. Under these assumptions, the drift and diffusion coefficients are found as

$$D^{(1)}\left(\tilde{E},\tilde{t}\right) = -A\tilde{E}(\tilde{t}) + k_1, \tag{12a}$$

$$D^{(2)}\left(\tilde{E},\tilde{t}\right) = k_2\tilde{E}(\tilde{t}), \tag{12b}$$

where

$$k_1 = \frac{3C_1FJ^2}{2G}, \quad k_2 = \frac{C_1B^2}{2}, \tag{13a}$$

$$A = \left(\frac{2\tau}{St^2} + \frac{2}{St}\right)\left(\frac{3\tau^{\frac{1}{2}}}{St} + \frac{1}{\tau^{\frac{1}{2}}}\right)^{-1},$$
$$B = \frac{2D^{\frac{1}{2}}}{St}\left(\frac{3\tau^{\frac{1}{2}}}{St} + \frac{1}{\tau^{\frac{1}{2}}}\right)^{-1},$$
$$F = \frac{2\tau}{St^2}\left(\frac{3\tau^{\frac{1}{2}}}{St} + \frac{1}{\tau^{\frac{1}{2}}}\right)^{-1}, \tag{13b}$$
$$G = \frac{1}{\tau^{\frac{1}{2}}}, \quad J = \frac{D^{\frac{1}{2}}}{\tau^{\frac{1}{2}}}.$$

Upon solving equation (11) for the steady-state profile with the provided coefficients, as done in Appendix B, we find

$$W_s\left(\tilde{E}\right) = a_0 \tilde{E}^{\frac{k_1}{k_2}-1} e^{-\frac{A}{k_2}\tilde{E}}, \tag{14a}$$

$$a_0 = \left[\int_0^\infty \tilde{E}^{\frac{k_1}{k_2}-1} e^{-\frac{A}{k_2}\tilde{E}}\, d\tilde{E}\right]^{-1}, \tag{14b}$$

where a_0 is found using the condition $\int_0^\infty W_s(\tilde{E})\, d\tilde{E} = 1$.

To compare the steady-state PDF model $W_s(\tilde{E})$ (equations (14a) and (14b)) with the simulation data for $\tilde{E}$ (shown in Figure 9(a)), we provide Figure 9(b). Since the PDFs for each value of St overlap in Figure 9(a), we multiply $\tilde{E}$ by $[\langle\langle E\rangle_P\rangle_T]|_{St=10.416}/[\langle\langle E\rangle_P\rangle_T]|_{St=3.472}$ and $[\langle\langle E\rangle_P\rangle_T]|_{St=31.250}/[\langle\langle E\rangle_P\rangle_T]|_{St=3.472}$ for $St = 10.416$ and 31.250, respectively, to provide a clear comparison of the steady-state PDF values for each St. To obtain parameters τ, C_1, and $D^{1/2}$, the model is fit to the simulation data for each value of St using the method of least squares. Additionally, three constraints are imposed to make the optimized parameters reasonably physical. The first constraint is the assumption $(3\tau^{1/2}/St + 1/\tau^{1/2})^{-1} \ll 1$, which coincides with making $\tau \geq 0$ as small as possible assuming the time scale of the colored noise is small with respect to $\hat{\tau}_{visc}$. In the second constraint, we consider the scaling of equation (10) and find $C_1 \sim 1$ assuming $\mathbf{Q}(t) \sim \mathcal{O}(1)$ under appropriate scaling. For the third constraint, we continue to assume the appropriate scaling of $\mathbf{Q}(t)$ and note that as $\tau \to 0$, equation (9c) reduces to $\tilde{\mathbf{u}}(t) \sim D^{1/2}\mathbf{Q}(t)$. To find the magnitude of $\tilde{\mathbf{u}}(t)$, we consider Figure 7 and note that to obtain $\langle K\rangle_z$ and E of similar magnitudes $\sim \mathcal{O}(1)$, E is scaled by an addition factor of $\hat{\rho}_f/\hat{\rho}_p = 0.001$. This means $K \sim 1000E$, and therefore, $\mathbf{u} \sim 1000^{1/2}\mathbf{v}$ and $\tilde{\mathbf{u}} \sim 1000^{1/2}\tilde{\mathbf{v}}$. Considering $\tilde{\mathbf{v}} \sim \mathcal{O}(1)$, as implied by the values of $E/\langle\langle E\rangle_P\rangle_T$ in Figure 9(a), we find that $\tilde{\mathbf{u}} \sim \mathcal{O}(1000^{1/2})$. Therefore, in order to maintain $\tilde{\mathbf{u}}(t) \sim D^{1/2}\mathbf{Q}(t)$ as $\tau \to 0$, we find that $D^{1/2} \sim 1000^{1/2} = 31.6228$.

TABLE V. The constrained parameters used to fit equations (14a) and (14b) to the simulation data using the method of least squares.

Variable	$St = 3.472$	$St = 10.416$	$St = 31.250$
τ	$1.385 \times 10^{-5} St$	$4.428 \times 10^{-6} St$	$2.937 \times 10^{-8} St$
C_1	0.106	1.000	1.000
$D^{1/2}$	56.914	32.351	146.069

As shown in Figure 9(b), the resulting steady-state PDF model $W_s(\tilde{E})$ is capable of matching the steady-state PDFs of $\tilde{E}$ for all three values of St. Parameters τ, C_1, and $D^{1/2}$ are varied for each value of St according to the values in Table V, which are deemed physically reasonable according to the previously described constraints. While the model is well-fitted for $St = 10.416$ and 31.250, we note that a slight deviation occurs between the simulation data and model for $St = 3.472$. We suggest this could be due to the shortening particle response time for decreased St. As previously investigated, particles closely follow the flow for reduced values of St. This means the velocity signals received by the particles from the flow are better correlated with the kinetic energy of the particles than for higher values of St. As a result, equation (9c) may be different, or more complex, in reality than the assumed form. Nonetheless, the model captures the steady-state PDFs of $\tilde{E}$ for the considered values of St and provides information for reduced-order modeling of particle dynamics in isotropic turbulence.

VII. SUMMARY AND CONCLUSIONS

We investigated flow and particle kinetic energies from three simulations of particle-laden, isotropic turbulence with varying St. Trends found in time-uncorrelated snapshots of the data were analyzed to develop an understanding of the particle dynamics on long time scales. Initially, a bias in the sampling of the flow by the particles was found with respect to $\langle K\rangle_F$ when comparing $\langle\alpha\rangle_T$, the average ratio of particles experiencing $\mathscr{K} < \langle K\rangle_F$, to $\langle\psi\rangle_T$, the average ratio of the domain where $K < \langle K\rangle_F$. After introducing dE/dt as a measure of general alignment and anti-alignment between particle velocity and acceleration vectors, a majority of particles losing kinetic energy over time were found to experience $\mathscr{K} < \langle K\rangle_F$. Additionally, the average particle kinetic energy of particles experiencing $\mathscr{K} < \langle K\rangle_F$ (i.e., $\langle E|_{\mathscr{K}<\langle K\rangle_F}\rangle_P$) was found to be lower than $\langle E\rangle_P$, suggesting that particles tend to move slower in regions where $\mathscr{K} < \langle K\rangle_F$. In considering these observations, it was proposed that particles accumulate in regions of low flow kinetic energy because they lose kinetic energy and slow down in such regions, which ultimately causes them to spend more time there.

An equation for the particle kinetic energy was then derived to further investigate the role of St in the pro-

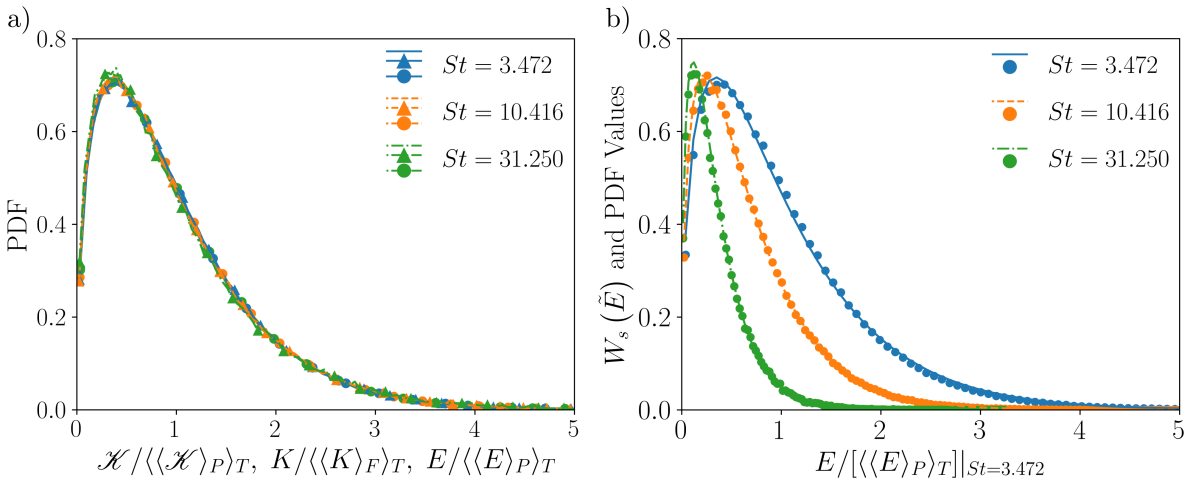

FIG. 9. a) The PDFs for $\mathscr{K}/\langle\langle\mathscr{K}\rangle_P\rangle_T$ (lines without overlaid shapes), $K/\langle\langle K\rangle_F\rangle_T$ (lines with overlaid dots), and $E/\langle\langle E\rangle_P\rangle_T$ (lines with overlaid triangles). b) The values of $W_s(\tilde{E})$ (equations (14a) and (14b); represented with lines) and the PDF values of $\tilde{E}$ from the simulations (represented with points) versus E scaled by $[\langle\langle E\rangle_P\rangle_T]|_{St=3.472}$.

posed particle behavior. *Strong* and *weak* events of particle kinetic energy decrease were defined with respect to whether particles lose kinetic energy in regions of $\mathscr{K} > E$ or $\mathscr{K} < E$, respectively. A correlation between St and the fraction of particles experiencing strong events over time was then hypothesized and agreement with simulation data was found, as the ratio of strong events counted over time rises with St. To unify the observed particle behavior, where particles must be responsive to the flow, with the idea that particles seem to lack response to the flow at high values of St, we proposed that St determines the time scale over which the proposed particle behavior may be observed. This hypothesis was in agreement with the simulation data: the proposed particle behavior became more difficult to observe as St increased, but the steady-state PDFs comparing $\mathscr{K}/\langle\langle K\rangle_F\rangle_T$ to $K/\langle\langle K\rangle_F\rangle_T$ in Figure 8 suggested that particles still followed the proposed particle behavior for the considered values of St.

Finally, scales for K, $\mathscr{K}$, and E were found such that the corresponding simulation data for all considered St collapsed onto similar PDFs (Figure 9(a)). Using the previously derived particle kinetic energy equation, a Fokker-Planck equation considering colored noise and long times after the initial state of the system was derived to model the steady-state PDF of $\tilde{E}$. Upon finding physically reasonable noise parameters (i.e., τ, C_1, and $D^{1/2}$) to fit the data corresponding to each St, the model was deemed valid and provided as a useful tool for reduced-order modeling of particle dynamics in isotropic turbulence.

Overall, the ideas proposed in this study yield additional insight into the physical mechanisms surrounding preferential concentration, and the stochastic model for particle kinetic energy serves as further evidence that such models can accurately capture the observed trends of particle-laden flows compared with higher fidelity methodologies. In the future, similar studies may be completed considering larger data sets of differing parameters, including higher particle (Re_p) and Taylor (Re_λ) Reynolds numbers, to further support the findings. We note that a previous study on preferential concentration [55] analyzed the scaling of particle clustering with the Taylor Reynolds number and found the overall trends were maintained across nearly a decade of Taylor Reynolds numbers, despite quantitative differences in the degree of clustering. This provides confidence that the stochastic formulation presented here could be extended to higher flow Reynolds numbers. Additionally, the effects of particle collision and two-way coupling could be investigated by applying the present analysis to existing high volume-fraction databases [43, 56], where such effects significantly influence particle motion and clustering. This would also provide an opportunity for reformulating the stochastic model to account for collisions and particle mutual hydrodynamic interactions. A challenge foreseen in this endeavor is incorporating further nonlinearity in the stochastic model (i.e., the correction f in the particle momentum equation would be a function of the volume fraction, Re_p, and may be far from unity); however, a comparison between the resulting conditional E distributions and those presented in this work could provide additional insight into the effects of high volume-fractions. Finally, connection and interpretation of the results with respect to flow variables commonly considered in preferential concentration, such as vorticity and strain rate, would broaden the ideas to a larger body of work. With the recent traction of machine learning for scientific investigation, efficient models of characteristic, physical trends have obtained additional popularity due to their support in areas of training and synthetic data creation. We look to apply the presented approach in

the future to non-isotropic flows and provide additional low-cost models to create a foundation for the testing and training of machine learning algorithms related to physical prediction in preferential concentration.

ACKNOWLEDGMENTS

KP was supported in-part by the Stanford Graduate Fellowship in Science and Engineering. This work was performed under the auspices of the U.S. Department of Energy by Lawrence Livermore National Laboratory under contract DE-AC52-07NA27344. Lawrence Livermore National Security, LLC. LLNL-JRNL-827712-DRAFT.

Appendix A: Derivation of the Fokker-Planck Equation with Colored Noise for Particle Kinetic Energy

Starting from equations (9a), (9b), and (9c), the temporal derivative of equation (9a) is calculated, and equation (9c) is substituted in to gain

$$\begin{aligned}\frac{d^2\tilde{E}(t)}{dt^2} =&-\frac{2}{St}\frac{d\tilde{E}(t)}{dt}-\frac{2}{St\tau}\tilde{\mathbf{u}}(t)\cdot\tilde{\mathbf{v}}(t)\\&+\frac{2D^{\frac{1}{2}}}{St\tau}\mathbf{Q}(t)\cdot\tilde{\mathbf{v}}(t)\\&+\frac{2}{St}\tilde{\mathbf{u}}(t)\cdot\frac{d\tilde{\mathbf{v}}(t)}{dt}.\end{aligned}\tag{A1}$$

Equations (9a) and (9b) are then used to obtain the expressions

$$\tilde{\mathbf{u}}(t)\cdot\tilde{\mathbf{v}}(t)=\frac{St}{2}\frac{d\tilde{E}}{dt}+\tilde{E},\tag{A2a}$$

$$\begin{aligned}\tilde{\mathbf{u}}(t)\cdot\frac{d\tilde{\mathbf{v}}(t)}{dt} =&\frac{1}{St}\tilde{\mathbf{u}}(t)\cdot\tilde{\mathbf{u}}(t)\\&-\frac{1}{2}\frac{d\tilde{E}(t)}{dt}-\frac{1}{St}\tilde{E},\end{aligned}\tag{A2b}$$

which are substituted into equation (A1) to obtain

$$\begin{aligned}\frac{d^2\tilde{E}(t)}{dt^2} =&-\left(\frac{3}{St}+\frac{1}{\tau}\right)\frac{d\tilde{E}(t)}{dt}\\&-\left(\frac{2}{St^2}+\frac{2}{St\tau}\right)\tilde{E}(t)\\&+\frac{2D^{\frac{1}{2}}}{St\tau}\mathbf{Q}(t)\cdot\tilde{\mathbf{v}}(t)\\&+\frac{2}{St^2}\tilde{\mathbf{u}}(t)\cdot\tilde{\mathbf{u}}(t).\end{aligned}\tag{A3}$$

Making the substitution $t=\tau^{\frac{1}{2}}\tilde{t}$, we gain

$$\begin{aligned}\frac{d^2\tilde{E}(\tilde{t})}{d\tilde{t}^2} =&-\left(\frac{3\tau^{\frac{1}{2}}}{St}+\frac{1}{\tau^{\frac{1}{2}}}\right)\frac{d\tilde{E}(\tilde{t})}{d\tilde{t}}\\&-\left(\frac{2\tau}{St^2}+\frac{2}{St}\right)\tilde{E}(\tilde{t})\\&+\frac{2D^{\frac{1}{2}}}{St}\mathbf{Q}(\tilde{t})\cdot\tilde{\mathbf{v}}(\tilde{t})\\&+\frac{2\tau}{St^2}\tilde{\mathbf{u}}(\tilde{t})\cdot\tilde{\mathbf{u}}(\tilde{t}).\end{aligned}\tag{A4}$$

Here, we assume $\left(3\tau^{\frac{1}{2}}/St+1/\tau^{\frac{1}{2}}\right)^{-1}\ll 1$, such that $d^2\tilde{E}(\tilde{t})/d\tilde{t}^2$ may be neglected. This allows for

$$\begin{aligned}\frac{d\tilde{E}(\tilde{t})}{d\tilde{t}} =&-A\tilde{E}(\tilde{t})+B\mathbf{Q}(\tilde{t})\cdot\tilde{\mathbf{v}}(\tilde{t})\\&+F\tilde{\mathbf{u}}(\tilde{t})\cdot\tilde{\mathbf{u}}(\tilde{t}),\end{aligned}\tag{A5}$$

where

$$A=\left(\frac{2\tau}{St^2}+\frac{2}{St}\right)\left(\frac{3\tau^{\frac{1}{2}}}{St}+\frac{1}{\tau^{\frac{1}{2}}}\right)^{-1},\tag{A6a}$$

$$B=\frac{2D^{\frac{1}{2}}}{St}\left(\frac{3\tau^{\frac{1}{2}}}{St}+\frac{1}{\tau^{\frac{1}{2}}}\right)^{-1},\tag{A6b}$$

$$F=\frac{2\tau}{St^2}\left(\frac{3\tau^{\frac{1}{2}}}{St}+\frac{1}{\tau^{\frac{1}{2}}}\right)^{-1}.\tag{A6c}$$

Then, integrating equation (A5) from $\tilde{t}$ to $\tilde{t}+\Delta\tilde{t}$ gains

$$\tilde{E}\left(\tilde{t}+\Delta\tilde{t}\right)-\tilde{E}\left(\tilde{t}\right)=-A\int_{\tilde{t}}^{\tilde{t}+\Delta\tilde{t}}\tilde{E}\left(\tau_1\right)\,d\tau_1+B\int_{\tilde{t}}^{\tilde{t}+\Delta\tilde{t}}\mathbf{Q}\left(\tau_1\right)\cdot\tilde{\mathbf{v}}\left(\tau_1\right)\,d\tau_1+F\int_{\tilde{t}}^{\tilde{t}+\Delta\tilde{t}}\tilde{\mathbf{u}}\left(\tau_1\right)\cdot\tilde{\mathbf{u}}\left(\tau_1\right)\,d\tau_1. \tag{A7}$$

In assuming the notation $\tilde{\mathbf{v}}(\tilde{t})\equiv\tilde{\mathbf{v}}(\tilde{E},\tilde{t})$, we write the Taylor expansions of $\tilde{\mathbf{v}}(\tilde{E}(\tau_1),\tau_1)$ and $\tilde{E}(\tau_1)$ about $\tilde{E}(\tilde{t})$ as

$$\begin{aligned}\tilde{\mathbf{v}}\left(\tilde{E}\left(\tau_1\right),\tau_1\right)=&\tilde{\mathbf{v}}\left(\tilde{E}\left(\tilde{t}\right),\tilde{t}\right)+\left(\tilde{E}\left(\tau_1\right)-\tilde{E}\left(\tilde{t}\right)\right)\left.\frac{\partial\tilde{\mathbf{v}}\left(\tilde{E},\tilde{t}\right)}{\partial\tilde{E}}\right|_{\tilde{E}=\tilde{E}\left(\tilde{t}\right)}\\&+\sum_{n_1=2}^{\infty}\frac{\left(\tilde{E}\left(\tau_1\right)-\tilde{E}\left(\tilde{t}\right)\right)^{n_1}}{n_1!}\left.\frac{\partial^{n_1}\tilde{\mathbf{v}}\left(\tilde{E},\tilde{t}\right)}{\partial\tilde{E}^{n_1}}\right|_{\tilde{E}=\tilde{E}\left(\tilde{t}\right)},\end{aligned} \tag{A8a}$$

$$\tilde{E}\left(\tau_1\right)=\tilde{E}\left(\tilde{t}\right)+\left(\tilde{E}\left(\tau_1\right)-\tilde{E}\left(\tilde{t}\right)\right). \tag{A8b}$$

Equations (A8a) and (A8b) are then used to write equation (A7) as

$$\begin{aligned}\tilde{E}\left(\tilde{t}+\Delta\tilde{t}\right)-\tilde{E}\left(\tilde{t}\right)=&-A\int_{\tilde{t}}^{\tilde{t}+\Delta\tilde{t}}\tilde{E}\left(\tilde{t}\right)\,d\tau_1+B\int_{\tilde{t}}^{\tilde{t}+\Delta\tilde{t}}\mathbf{Q}\left(\tau_1\right)\cdot\tilde{\mathbf{v}}\left(\tilde{E}\left(\tilde{t}\right),\tilde{t}\right)\,d\tau_1+F\int_{\tilde{t}}^{\tilde{t}+\Delta\tilde{t}}\tilde{\mathbf{u}}\left(\tau_1\right)\cdot\tilde{\mathbf{u}}\left(\tau_1\right)\,d\tau_1\\&+\int_{\tilde{t}}^{\tilde{t}+\Delta\tilde{t}}\left(B\mathbf{Q}\left(\tau_1\right)\cdot\left.\frac{\partial\tilde{\mathbf{v}}\left(\tilde{E},\tilde{t}\right)}{\partial\tilde{E}}\right|_{\tilde{E}=\tilde{E}\left(\tilde{t}\right)}-A\right)\left(\tilde{E}\left(\tau_1\right)-\tilde{E}\left(\tilde{t}\right)\right)\,d\tau_1\\&+B\sum_{n_1=2}^{\infty}\left[\int_{\tilde{t}}^{\tilde{t}+\Delta\tilde{t}}\left(\mathbf{Q}\left(\tau_1\right)\cdot\left.\frac{\partial^{n_1}\tilde{\mathbf{v}}\left(\tilde{E},\tilde{t}\right)}{\partial\tilde{E}^{n_1}}\right|_{\tilde{E}=\tilde{E}\left(\tilde{t}\right)}\right)\frac{\left(\tilde{E}\left(\tau_1\right)-\tilde{E}\left(\tilde{t}\right)\right)^{n_1}}{n_1!}\,d\tau_1\right].\end{aligned} \tag{A9}$$

To find an expression for $\tilde{E}(\tau_1)-\tilde{E}(\tilde{t})$, we change dummy variable τ_1 to τ_2 in equation (A9), and then substitute in τ_1 for $\tilde{t}+\Delta\tilde{t}$. Upon doing so, we gain an equation for $\tilde{E}(\tau_1)-\tilde{E}(\tilde{t})$, which is substituted into equation (A9) to obtain

$$\begin{aligned}\tilde{E}\left(\tilde{t}+\Delta\tilde{t}\right)-\tilde{E}\left(\tilde{t}\right)=&-A\int_{\tilde{t}}^{\tilde{t}+\Delta\tilde{t}}\tilde{E}\left(\tilde{t}\right)\,d\tau_1+B\int_{\tilde{t}}^{\tilde{t}+\Delta\tilde{t}}\mathbf{Q}\left(\tau_1\right)\cdot\tilde{\mathbf{v}}\left(\tilde{E}\left(\tilde{t}\right),\tilde{t}\right)\,d\tau_1+F\int_{\tilde{t}}^{\tilde{t}+\Delta\tilde{t}}\tilde{\mathbf{u}}\left(\tau_1\right)\cdot\tilde{\mathbf{u}}\left(\tau_1\right)\,d\tau_1\\&-A\int_{\tilde{t}}^{\tilde{t}+\Delta\tilde{t}}\int_{\tilde{t}}^{\tau_1}\left(B\mathbf{Q}\left(\tau_1\right)\cdot\left.\frac{\partial\tilde{\mathbf{v}}\left(\tilde{E},\tilde{t}\right)}{\partial\tilde{E}}\right|_{\tilde{E}=\tilde{E}\left(\tilde{t}\right)}-A\right)\tilde{E}\left(\tilde{t}\right)\,d\tau_2d\tau_1\\&+B\int_{\tilde{t}}^{\tilde{t}+\Delta\tilde{t}}\int_{\tilde{t}}^{\tau_1}\left(B\mathbf{Q}\left(\tau_1\right)\cdot\left.\frac{\partial\tilde{\mathbf{v}}\left(\tilde{E},\tilde{t}\right)}{\partial\tilde{E}}\right|_{\tilde{E}=\tilde{E}\left(\tilde{t}\right)}-A\right)\left(\mathbf{Q}\left(\tau_2\right)\cdot\tilde{\mathbf{v}}\left(\tilde{E}\left(\tilde{t}\right),\tilde{t}\right)\right)\,d\tau_2d\tau_1+\text{H.O.T.},\end{aligned} \tag{A10}$$

where only the lower-order terms contributing to this analysis have been written to preserve simplicity. While further recursive substitutions may be made in the higher-order terms, we find this form sufficient for our derivation.

1. The Drift Coefficient

To calculate the drift coefficient, we use [52]

$$D^{(1)}\left(\tilde{E},\tilde{t}\right)=\lim_{\Delta\tilde{t}\to0}\frac{\overline{\tilde{E}\left(\tilde{t}+\Delta\tilde{t}\right)-\tilde{E}\left(\tilde{t}\right)}}{\Delta\tilde{t}}, \tag{A11}$$

and assume [54]

$$\overline{Q_i\left(\tilde{t}\right)}=0, \tag{A12a}$$

$$\overline{Q_i\left(\tilde{t}_1\right)Q_j\left(\tilde{t}_2\right)}=C_1\delta_{ij}\delta\left(\tilde{t}_1-\tilde{t}_2\right), \tag{A12b}$$

$$\overline{Q_{i_1}\left(\tilde{t}_1\right)Q_{i_2}\left(\tilde{t}_2\right)\,...\,Q_{i_{2n-1}}\left(\tilde{t}_{2n-1}\right)}=0, \tag{A12c}$$

$$\overline{Q_{i_1}\left(\tilde{t}_1\right) Q_{i_2}\left(\tilde{t}_2\right)\ \ldots\ Q_{i_{2n}}\left(\tilde{t}_{2n}\right)} = C_1^n \times \sum_{P_d} \delta\left(\tilde{t}_{j_1}-\tilde{t}_{j_2}\right)\ \ldots\ \delta\left(\tilde{t}_{j_{2n-1}}-\tilde{t}_{j_{2n}}\right), \tag{A12d}$$

where $n = 2, 3, 4, \ldots$, $Q_i(\tilde{t})$ are the components of $\mathbf{Q}(\tilde{t})$, $\delta_{ij} = \mathbf{I}$ and $\delta(\tilde{t}_1 - \tilde{t}_2)$ are forms of the Dirac delta function, and P_d is the $(2n)!/(2^n n!)$ permutations of subtracted "$\tilde{t}$"s in the Dirac delta functions. We now use equation (A10) to find $\tilde{E}(\tilde{t}+\Delta\tilde{t}) - \tilde{E}(\tilde{t})$ by simplifying the ensemble average of each term in the equation using the properties from equation (A12). In doing so, the first term of equation (A10) becomes

$$-A\int_{\tilde{t}}^{\tilde{t}+\Delta\tilde{t}} \tilde{E}\left(\tilde{t}\right)\ d\tau_1 = -A\tilde{E}\left(\tilde{t}\right)\Delta\tilde{t}. \tag{A13}$$

Noting that the ensemble average of the second term simplifies to zero due to $\overline{Q_i(\tilde{t})} = 0$, we simplify the third term by first making the substitution $t = \tau^{\frac{1}{2}}\tilde{t}$ in equation (9c) to gain

$$\frac{d\tilde{\mathbf{u}}\left(\tilde{t}\right)}{d\tilde{t}} = -G\tilde{\mathbf{u}}\left(\tilde{t}\right) + J\mathbf{Q}\left(\tilde{t}\right), \tag{A14}$$

where $G = 1/\tau^{\frac{1}{2}}$ and $J = D^{\frac{1}{2}}/\tau^{\frac{1}{2}}$. Equation (A14) is then solved to find

$$\tilde{\mathbf{u}}\left(\tilde{t}\right) = \tilde{\mathbf{u}}_0 e^{-G\tilde{t}} + Je^{-G\tilde{t}}\int_0^{\tilde{t}} e^{G\tilde{t}'}\mathbf{Q}\left(\tilde{t}'\right)\ d\tilde{t}', \tag{A15}$$

where $\tilde{\mathbf{u}}_0 = \tilde{\mathbf{u}}(0)$. Assuming long enough times $\tilde{t}$, we neglect the first term in equation (A15) due to its decay over time. We then write the ensemble average of the third term from equation (A10) as

$$F\int_{\tilde{t}}^{\tilde{t}+\Delta\tilde{t}} \overline{\tilde{\mathbf{u}}\left(\tau_1\right)\cdot\tilde{\mathbf{u}}\left(\tau_1\right)}\, d\tau_1 = FJ^2\int_{\tilde{t}}^{\tilde{t}+\Delta\tilde{t}} e^{-2G\tau_1}\int_0^{\tau_1}\int_0^{\tau_1} e^{G\left(\tilde{t}_1'+\tilde{t}_2'\right)}\overline{\mathbf{Q}\left(\tilde{t}_1'\right)\cdot\mathbf{Q}\left(\tilde{t}_2'\right)}\, d\tilde{t}_2' d\tilde{t}_1'\, d\tau_1, \tag{A16}$$

which is reduced using the properties in equation (A12) to

$$F\int_{\tilde{t}}^{\tilde{t}+\Delta\tilde{t}} \overline{\tilde{\mathbf{u}}\left(\tau_1\right)\cdot\tilde{\mathbf{u}}\left(\tau_1\right)}\, d\tau_1 = \frac{3C_1FJ^2}{2G}\left[\frac{e^{-2G\left(\tilde{t}+\Delta\tilde{t}\right)} - e^{-2G\tilde{t}}}{2G} + \Delta\tilde{t}\right]. \tag{A17}$$

While the fourth term in equation (A10) reduces to $\mathcal{O}(\Delta\tilde{t}^2)$, the ensemble average of the fifth term is reduced to

$$\begin{aligned} &B\int_{\tilde{t}}^{\tilde{t}+\Delta\tilde{t}}\int_{\tilde{t}}^{\tau_1} \overline{\left(B\mathbf{Q}\left(\tau_1\right)\cdot\left.\frac{\partial\tilde{\mathbf{v}}\left(\tilde{E},\tilde{t}\right)}{\partial\tilde{E}}\right|_{\tilde{E}=\tilde{E}\left(\tilde{t}\right)} - A\right)\left(\mathbf{Q}\left(\tau_2\right)\cdot\tilde{\mathbf{v}}\left(\tilde{E}\left(\tilde{t}\right),\tilde{t}\right)\right)}\, d\tau_2 d\tau_1 \\ &= B^2\int_{\tilde{t}}^{\tilde{t}+\Delta\tilde{t}}\int_{\tilde{t}}^{\tau_1} \overline{\left(\mathbf{Q}\left(\tau_1\right)\cdot\left.\frac{\partial\tilde{\mathbf{v}}\left(\tilde{E},\tilde{t}\right)}{\partial\tilde{E}}\right|_{\tilde{E}=\tilde{E}\left(\tilde{t}\right)}\right)\left(\mathbf{Q}\left(\tau_2\right)\cdot\tilde{\mathbf{v}}\left(\tilde{E}\left(\tilde{t}\right),\tilde{t}\right)\right)}\, d\tau_2 d\tau_1, \end{aligned} \tag{A18}$$

where the integrand on the right side of the equation can be expanded and simplified using the previous properties to

$$\overline{\left(\mathbf{Q}\left(\tau_1\right)\cdot\left.\frac{\partial\tilde{\mathbf{v}}\left(\tilde{E},\tilde{t}\right)}{\partial\tilde{E}}\right|_{\tilde{E}=\tilde{E}\left(\tilde{t}\right)}\right)\left(\mathbf{Q}\left(\tau_2\right)\cdot\tilde{\mathbf{v}}\left(\tilde{E}\left(\tilde{t}\right),\tilde{t}\right)\right)} = \frac{C_1}{2}\delta\left(\tau_1-\tau_2\right). \tag{A19}$$

Therefore, equation (A18) becomes

$$B\int_{\tilde{t}}^{\tilde{t}+\Delta\tilde{t}}\int_{\tilde{t}}^{\tau_1} \overline{\left(B\mathbf{Q}\left(\tau_1\right)\cdot\left.\frac{\partial\tilde{\mathbf{v}}\left(\tilde{E},\tilde{t}\right)}{\partial\tilde{E}}\right|_{\tilde{E}=\tilde{E}\left(\tilde{t}\right)} - A\right)\left(\mathbf{Q}\left(\tau_2\right)\cdot\tilde{\mathbf{v}}\left(\tilde{E}\left(\tilde{t}\right),\tilde{t}\right)\right)}\, d\tau_2 d\tau_1 = \frac{C_1B^2\Delta\tilde{t}}{2}\left[H\left(\Delta\tilde{t}\right) - H\left(0\right)\right]. \tag{A20}$$

Beyond the fifth term, terms become of order $\mathcal{O}(\Delta\tilde{t}^2)$ or smaller due to the increasing number of integrals and insufficient production of Dirac delta functions in the integrands from the correlations between the components of $\mathbf{Q}(\tilde{t})$. We neglect these terms and write the ensemble average of equation (A10) as

$$\overline{\tilde{E}\left(\tilde{t}+\Delta\tilde{t}\right)-\tilde{E}\left(\tilde{t}\right)} = -A\tilde{E}\left(\tilde{t}\right)\Delta\tilde{t} + \frac{3C_1FJ^2}{2G}\left[\frac{e^{-2G\left(\tilde{t}+\Delta\tilde{t}\right)}-e^{-2G\tilde{t}}}{2G}+\Delta\tilde{t}\right] + \frac{C_1B^2\Delta\tilde{t}}{2}\left[H\left(\Delta\tilde{t}\right)-H\left(0\right)\right]+\mathcal{O}\left(\Delta\tilde{t}^2\right), \tag{A21}$$

and the drift coefficient becomes

$$D^{(1)}\left(\tilde{E},\tilde{t}\right) = -A\tilde{E}\left(\tilde{t}\right) + \frac{3C_1FJ^2}{2G}\left[1-e^{-2G\tilde{t}}\right] + \frac{C_1B^2}{2}\left[\lim_{\Delta\tilde{t}\to 0}\left[H\left(\Delta\tilde{t}\right)\right]-H\left(0\right)\right]. \tag{A22}$$

Since the limit $\lim_{\Delta\tilde{t}\to 0}[H(\Delta\tilde{t})]$ is undefined and the definition of $H(0)$ is not universally accepted, we let $C_2 = \lim_{\Delta\tilde{t}\to 0}[H(\Delta\tilde{t})] - H(0)$ to accommodate the various interpretations of the Heaviside function. We note that our interpretation is $C_2 = 0$, but retain C_2 in this derivation for generality. Additionally, we note that after long enough time $\tilde{t}$, contributions from $e^{-2G\tilde{t}}$ may be neglected. Therefore, we write the drift coefficient as

$$D^{(1)}\left(\tilde{E},\tilde{t}\right) = -A\tilde{E}\left(\tilde{t}\right) + k_1, \tag{A23}$$

where $k_1 = 3C_1FJ^2/2G + C_1C_2B^2/2$.

2. The Diffusion Coefficient

To calculate the diffusion coefficient, we use [52]

$$D^{(2)}\left(\tilde{E},\tilde{t}\right) = \lim_{\Delta\tilde{t}\to 0}\frac{\overline{\left[\tilde{E}\left(\tilde{t}+\Delta\tilde{t}\right)-\tilde{E}\left(\tilde{t}\right)\right]^2}}{2\Delta\tilde{t}}, \tag{A24}$$

and again assume the properties in equation (A12). We can use equation (A10) to find $\overline{[\tilde{E}(\tilde{t}+\Delta\tilde{t})-\tilde{E}(\tilde{t})]^2}$ and consider each of the resulting terms independently. The resulting expression for $\overline{[\tilde{E}(\tilde{t}+\Delta\tilde{t})-\tilde{E}(\tilde{t})]^2}$ will not be provided due to its length, but we note that only one term will be of order $\mathcal{O}(\Delta\tilde{t})$, and therefore

$$\overline{\left[\tilde{E}\left(\tilde{t}+\Delta\tilde{t}\right)-\tilde{E}\left(\tilde{t}\right)\right]^2} = B^2\int_{\tilde{t}}^{\tilde{t}+\Delta\tilde{t}}\int_{\tilde{t}}^{\tilde{t}+\Delta\tilde{t}}\overline{\left(\mathbf{Q}\left(\tau_1^{(1)}\right)\cdot\tilde{\mathbf{v}}\left(\tilde{E}\left(\tilde{t}\right),\tilde{t}\right)\right)\left(\mathbf{Q}\left(\tau_1^{(2)}\right)\cdot\tilde{\mathbf{v}}\left(\tilde{E}\left(\tilde{t}\right),\tilde{t}\right)\right)}\,d\tau_1^{(1)}d\tau_1^{(2)}+\mathcal{O}\left(\Delta\tilde{t}^2\right). \tag{A25}$$

By expanding and simplifying the integrand of equation (A25), we gain

$$\overline{\left(\mathbf{Q}\left(\tau_1^{(1)}\right)\cdot\tilde{\mathbf{v}}\left(\tilde{E}\left(\tilde{t}\right),\tilde{t}\right)\right)\left(\mathbf{Q}\left(\tau_1^{(2)}\right)\cdot\tilde{\mathbf{v}}\left(\tilde{E}\left(\tilde{t}\right),\tilde{t}\right)\right)} = C_1\delta\left(\tau_1^{(1)}-\tau_1^{(2)}\right)\tilde{E}\left(\tilde{t}\right), \tag{A26}$$

and therefore,

$$\overline{\left[\tilde{E}\left(\tilde{t}+\Delta\tilde{t}\right)-\tilde{E}\left(\tilde{t}\right)\right]^2} = C_1B^2\tilde{E}\left(\tilde{t}\right)\Delta\tilde{t}+\mathcal{O}\left(\Delta\tilde{t}^2\right). \tag{A27}$$

Because all other terms are either $\mathcal{O}(\Delta\tilde{t}^2)$ or less, we define the diffusion coefficient as

$$D^{(2)}\left(\tilde{E},\tilde{t}\right) = k_2\tilde{E}\left(\tilde{t}\right). \tag{A28}$$

where $k_2 = C_1B^2/2$.

Appendix B: The Fokker-Planck Equation and the Steady-State PDF Profile:

With the coefficients defined, we write the Fokker-Planck equation using equation (11) as

$$\frac{\partial W\left(\tilde{E},\tilde{t}\right)}{\partial\tilde{t}} = -\frac{\partial}{\partial\tilde{E}}\left[\left(-A\tilde{E}+k_1\right)W\left(\tilde{E},\tilde{t}\right)\right] + \frac{\partial^2}{\partial\tilde{E}^2}\left[\left(k_2\tilde{E}\right)W\left(\tilde{E},\tilde{t}\right)\right]. \tag{B1}$$

To solve equation (B1) for the steady-state PDF profile, we first set $\partial W(\tilde{E},\tilde{t})/\partial\tilde{t} = 0$ and integrate once in $\tilde{E}$ from 0 to ∞ to gain

$$0 = \left[\left(A\tilde{E} - k_1 + k_2\right)W + k_2\tilde{E}\frac{\partial W}{\partial\tilde{E}}\right]_0^{\infty}. \tag{B2}$$

Here, we assume $W \to 0$ and $\partial W/\partial\tilde{E} \to 0$ faster than $\tilde{E} \to \infty$. Therefore, we find

$$0 = \left[\left(A\tilde{E} - k_1 + k_2\right)W + k_2\tilde{E}\frac{\partial W}{\partial\tilde{E}}\right]\Bigg|_0. \tag{B3}$$

With this information, we again assume $\partial W(\tilde{E},\tilde{t})/\partial\tilde{t} = 0$ and integrate equation (B1) once in $\tilde{E}$ from 0 to $\tilde{E}$ to gain

$$0 = \left[\left(A\tilde{E} - k_1 + k_2\right)W + k_2\tilde{E}\frac{\partial W}{\partial\tilde{E}}\right]_0^{\tilde{E}}, \tag{B4}$$

and therefore, using equation (B3), we gain

$$0 = \left(\frac{A}{k_2} + \frac{1 - k_1/k_2}{\tilde{E}}\right)W + \frac{\partial W}{\partial\tilde{E}}. \tag{B5}$$

The solution to equation (B5) is written as

$$W = a_0\tilde{E}^{\frac{k_1}{k_2}-1}e^{-\frac{A}{k_2}\tilde{E}}, \tag{B6}$$

where a_0 is found using the condition $\int_0^{\infty} W\, d\tilde{E} = 1$ as

$$a_0 = \left[\int_0^{\infty} \tilde{E}^{\frac{k_1}{k_2}-1}e^{-\frac{A}{k_2}\tilde{E}}\, d\tilde{E}\right]^{-1}. \tag{B7}$$

[1] K. D. Squires and J. K. Eaton, Phys. Fluids A-Fluid **3**, 1169 (1991).
[2] M. B. Pinsky and A. P. Khain, J. Aerosol Sci. **28**, 1177 (1997).
[3] R. A. Shaw, W. C. Reade, L. R. Collins, and J. Verlinde, J. Atmos. Sci. **55**, 1965 (1998).
[4] R. A. Shaw, Annu. Rev. Fluid Mech. **35**, 183 (2003).
[5] J. Reveillon and F.-X. Demoulin, J. Fluid Mech. **583**, 273 (2007).
[6] D. M. Lewis and T. J. Pedley, J. Theor. Biol. **210**, 347 (2001).
[7] R. Monchaux, M. Bourgoin, and A. Cartellier, Int. J. Multiphas. Flow **40**, 1 (2012).
[8] S. Balachandar and J. K. Eaton, Annu. Rev. Fluid Mech. **42**, 111 (2010).
[9] J. A. K. Horwitz and A. Mani, Int. J. Multiphas. Flow **101**, 74 (2018).
[10] M. R. Maxey, J. Fluid Mech. **174**, 441 (1987).
[11] R. Chein and J. N. Chung, Int. J. Multiphase Flow **13**, 785 (1987).
[12] J. K. Eaton and J. R. Fessler, Int. J. Multiphase Flow **20**, 169 (1994).
[13] J. Chun, D. L. Koch, S. L. Rani, A. Ahluwalia, and L. R. Collins, J. Fluid Mech. **536**, 216 (2005).
[14] L. I. Zaichik and V. M. Alipchenkov, Phys. Fluids **19** (2007), 113308.
[15] L. I. Zaichik and V. M. Alipchenkov, Phys. Fluids **15**, 1776 (2003).
[16] S. Sundaram and L. R. Collins, J. Fluid Mech. **335**, 75 (1997).
[17] W. C. Reade and L. R. Collins, Phys. Fluids **12**, 2530 (2000).
[18] J. Bec, L. Biferale, M. Cencini, A. Lanotte, S. Musacchio, and F. Toschi, Phys. Rev. Lett. **98** (2007), 084502.
[19] A. D. Bragg and L. R. Collins, New J. Phys. **16** (2014), 055013.
[20] J. Bec, L. Biferale, G. Boffetta, A. Celani, M. Cencini, A. Lanotte, S. Musacchio, and F. Toschi, J. Fluid Mech. **550**, 349 (2006).
[21] H. Yoshimoto and S. Goto, J. Fluid Mech. **577**, 275 (2007).
[22] K. Gustavsson and B. Mehlig, EPL **96** (2011), 60012.
[23] K. Duncan, B. Mehlig, S. Östlund, and M. Wilkinson, Phys. Rev. Lett. **95** (2005), 240602.
[24] M. Wilkinson and B. Mehlig, Europhys. Lett. **71**, 186 (2005).
[25] M. Wilkinson, B. Mehlig, S. Östlund, and K. P. Duncan, Phys. Fluids **19** (2007), 113303.
[26] K. Gustavsson, E. Meneguz, M. Reeks, and B. Mehlig, New J. Phys. **14** (2012), 115017.
[27] L. Chen, S. Goto, and J. C. Vassilicos, J. Fluid Mech. **553**, 143 (2006).
[28] S. Goto and J. C. Vassilicos, Phys. Fluids **18**, 115103 (2006).
[29] S. Goto and J. C. Vassilicos, Phys. Rev. Lett. **100** (2008), 054503.
[30] S. W. Coleman and J. C. Vassilicos, Phys. Fluids **21**, 113301 (2009).
[31] M. Obligado, T. Teitelbaum, A. Cartellier, P. Mininni, and M. Bourgoin, J. Turbul. **15**, 293 (2014).
[32] B. Ray and L. R. Collins, J. Fluid Mech. **720**, 192 (2013).
[33] M. Wilkinson and B. Mehlig, Phys. Rev. E **68** (2003), 040101.
[34] K. Gustavsson and B. Mehlig, Adv. Phys. **65**, 1 (2016).
[35] H. Sigurgeirsson and A. M. Stuart, Phys. Fluids **14**, 4352 (2002).
[36] M. G. Pai and S. Subramaniam, J. Fluid Mech. **700**, 29 (2012).
[37] A. M. Lattanzi, V. Tavanashad, S. Subramaniam, and J. Capecelatro, J. Fluid Mech. **903**, A7 (2020).
[38] A. J. Banko, L. V. ne, J. H. Kim, M. Esmaily, and J. K. Eaton, J. Quant. Spectrosc. Ra. **226**, 1 (2019).

[39] A. Bhatnagar, A. Gupta, D. Mitra, and R. Pandit, Phys. Rev. E **97** (2018), 033102.
[40] H. Xu, A. Pumir, G. Falkovich, E. Bodenschatz, M. Shats, H. Xia, N. Francois, and G. Boffetta, P. Natl. Acad. Sci. USA **111**, 7558 (2014).
[41] T. Grafke, A. Frishman, and G. Falkovich, Phys. Rev. E **91** (2015), 043022.
[42] Q. Pan, H. Xiang, Z. Wang, H. I. Andersson, and L. Zhao, Phys. Fluids **32** (2020), 073307.
[43] S. Tenneti, M. Mehrabadi, and S. Subramaniam, J. Fluid Mech. **788**, 695 (2016).
[44] V. Garzó, S. Tenneti, S. Subramaniam, and C. M. Hrenya, J. Fluid Mech. **712**, 129 (2012).
[45] L. Zhao, H. I. Andersson, and J. J. J. Gillissen, J. Fluid Mech. **715**, 32 (2013).
[46] K. D. Squires and J. K. Eaton, Phys. Fluids A **2**, 1191 (1990).
[47] J. Pozorski and S. V. Apte, Int. J. Multiphas. Flow **35**, 118 (2009).
[48] M. Esmaily-Moghadam and A. Mani, Phys. Rev. Fluids **1** (2016), 084202.
[49] S. L. Rani, R. Dhariwal, and D. L. Koch, J. Fluid Mech. **756**, 870 (2014).
[50] R. Dhariwal, S. L. Rani, and D. L. Koch, J. Fluid Mech. **813**, 205 (2017).
[51] S. L. Rani, V. K. Gupta, and D. L. Koch, J. Fluid Mech. **871**, 450 (2019).
[52] W. T. Coffey and Y. P. Kalmykov, *The Langevin Equation with Applications to Stochastic Problems in Physics, Chemistry and Electrical Engineering* (World Scientific Publishing Co., 5 Toh Tuck Link, Singapore 596224, 2017).
[53] P. Hänggi, in *Noise in Nonlinear Dynamical Systems, Volume 1: Theory of Continuous Fokker-Planck Systems*, edited by F. Moss and P. V. E. McClintock (Cambridge University Press, The Edinburgh Building, Cambridge CB2 8RU, UK, 1989) Chap. 9, pp. 307–328.
[54] H. Risken, *The Fokker-Planck Equation: Methods of Solution and Applications* (Springer, New York, New York, 1989).
[55] P. J. Ireland and A. D. Bragg, J. Fluid Mech. **796**, 617 (2016).
[56] V. Tavanashad, A. Passalacqua, and S. Subramaniam, Int. J. Multiphas. Flow **135** (2021), 103533.